Monthly Notices
of the
ROYAL ASTRONOMICAL SOCIETY

MNRAS **458,** 1891–1908 (2016)
Advance Access publication 2016 February 26

doi:10.1093/mnras/stw449

Spatially resolved galactic wind in lensed galaxy RCSGA 032727-132609

Rongmon Bordoloi,[1,2★†] Jane R. Rigby,[3] Jason Tumlinson,[1] Matthew B. Bayliss,[4,5] Keren Sharon,[6] Michael G. Gladders[7,8] and Eva Wuyts[9]

[1]*Space Telescope Science Institute, 3700 San Martin Drive, Baltimore, MD 21218, USA*
[2]*MIT-Kavli Center for Astrophysics and Space Research, 77 Massachusetts Avenue, Cambridge, MA 02139, USA*
[3]*NASA Goddard Space Flight Center, Code 665, Greenbelt, MD 20771, USA*
[4]*Department of Physics, Harvard University, 17 Oxford St, Cambridge, MA 02138, USA*
[5]*Harvard-Smithsonian Center for Astrophysics, 60 Garden Street, Cambridge, MA 02138, USA*
[6]*Department of Astronomy and Astrophysics, University of Michigan, 500 Church Street, Ann Arbor, MI 48109, USA*
[7]*Department of Astronomy and Astrophysics, University of Chicago, 5640 South Ellis Avenue, Chicago, IL 60637, USA*
[8]*Kavli Institute for Cosmological Physics at the University of Chicago*
[9]*Max-Planck-Institut f'ur extraterrestrische Physik, Postfach 1312, Giessenbachstr., D-85741 Garching, Germany*

Accepted 2016 February 24. Received 2016 February 24; in original form 2015 September 9

ABSTRACT

We probe the spatial distribution of outflowing gas along four lines of sight separated by up to 6 kpc in a gravitationally lensed star-forming galaxy at $z = 1.70$. Using Mg II and Fe II emission and absorption as tracers, we find that the clumps of star formation are driving galactic outflows with velocities of -170 to -250 km s^{-1}. The velocities of Mg II emission are redshifted with respect to the systemic velocities of the galaxy, consistent with being back-scattered. By contrast, the Fe II fluorescent emission lines are either slightly blueshifted or at the systemic velocity of the galaxy. Taken together, the velocity structure of the Mg II and Fe II emission is consistent with arising through scattering in galactic winds. Assuming a thin shell geometry for the outflowing gas, the estimated masses carried out by these outflows are large ($\gtrsim$30–50 M$_\odot$ yr^{-1}), with mass loading factors several times the star formation rate. Almost 20 per cent to 50 per cent of the blueshifted absorption probably escapes the gravitational potential of the galaxy. In this galaxy, the outflow is 'locally sourced', that is, the properties of the outflow in each line of sight are dominated by the properties of the nearest clump of star formation; the wind is not global to the galaxy. The mass outflow rates and the momentum flux carried out by outflows in individual star-forming knots of this object are comparable to that of starburst galaxies in the local Universe.

Key words: galaxies: evolution – galaxies: high-redshift – intergalactic medium – ultraviolet: ISM.

1 INTRODUCTION

In the last decade, our understanding of the formation and evolution of galaxies over cosmic time has been significantly enhanced by large-scale spectroscopic galaxy surveys. These surveys have unearthed a detailed picture of the properties of the galaxies, establishing their bi-modal distribution in the colour–magnitude diagram (Blanton et al. 2003), mass–metallicity relation (Tremonti et al. 2004) and the galaxy stellar mass function to high precision (Bell et al. 2003). Surveys observing galaxies over a broad range of cosmic time have identified that the average star formation rates (SFR) drop several-fold (Daddi et al. 2007; Noeske et al. 2007), the fraction of galaxies on the red sequence more than doubles (Faber et al. 2007; Brammer et al. 2011), and red galaxies grow passively (Patel et al. 2013) while star-forming discs become more ordered (Kassin et al. 2012).

Theoretical models explaining these galaxy properties as well as the observed metal enrichment of the intergalactic medium (IGM; Adelberger et al. 2005; Cooksey et al. 2010), consistently invoke feedback mechanisms to account for the discrepancies between theory and observations. These processes, and in particular galactic outflows are thought to drive the mass–metallicity relation, enrich the IGM (Bordoloi et al. 2011; Tumlinson et al. 2011; Zhu & Ménard 2013; Bordoloi et al. 2014c; Werk et al. 2014), and regulate star formation and black hole growth (Gabor et al. 2011).

In the local Universe, hot outflowing galactic winds are observed with X-ray emission, and cooler phases of the outflowing gas are detected via optical emission lines such as H α (e.g. Lehnert & Heckman 1996), and in 'down-the-barrel' observations of absorption lines against the galaxy's stellar continuum (see Veilleux, Cecil

★ E-mail: rongmon.bordoloi@gmail.com
† Hubble Fellow.

& Bland-Hawthorn 2005 for review). The kinematics and column density of the cool (100–1000 K) gas entrained in the hot outflowing gas of the local dwarf starbursts and luminous infrared galaxies up to $z \sim 0.5$ are detected using the blueshifed Na I D λλ5890, 5896 doublet (Heckman et al. 2000; Martin 2005; Rupke, Veilleux & Sanders 2005).

At $z \sim 3$, using UV transitions such as Si II λ 1206 and C IV λλ1548, 1550 blueshifted outflowing gas with velocities of hundreds of km s^{-1} have been observed in the spectra of Lyman break galaxies (LBG; Shapley et al. 2003). Outflows have also been detected at $z \sim 2$ using extended Hα emission wings (Newman et al. 2012; Förster Schreiber et al. 2014; Genzel et al. 2014). At $z \sim 1$, outflowing gas has been found by several studies (Weiner et al. 2009; Martin et al. 2012; Rubin et al. 2012; Bordoloi et al. 2014b) to be largely ubiquitous. These large-scale outflows are biconical in morphology (Bordoloi et al. 2011; Martin et al. 2012; Bordoloi et al. 2014a,b; Rubin et al. 2014) and exhibit resonant Mg II and fine-structure Fe II emission lines (Erb et al. 2012; Kornei et al. 2013).

Moreover, studies of down-the-barrel spectra of individual galaxies have also yielded evidence of redshifted inflowing absorption in Mg II and Fe II transitions (Rubin et al. 2011; Kornei et al. 2012; Martin et al. 2012). The covering fraction of inflowing gas (not masked by outflows) around these galaxies has been found to be small (≈ 6 per cent). These studies have identified galaxies with large concentration of massive stars to be driving strong outflows (Kornei et al. 2012, 2013; Bordoloi et al. 2014b), consistent with theoretical studies requiring massive star clusters to drive galactic outflows (Murray, Ménard & Thompson 2011). To understand these outflows, it is particularly important to understand the spatial scales involved and the mass outflow rate; the latter is a crucial, as-yet-poorly constrained parameter in galaxy evolution models (Davé, Finlator & Oppenheimer 2012).

Previous studies have provided constraints on the spatial scales of the outflows, particularly as traced by emission from the resonant doublet Mg II 2796, 2803 Å. Erb et al. (2012) constructed a two-dimensional composite spectrum of 33 galaxies that show Mg II emission; the stacked Mg II is slightly more extended than the continuum at distances of 0.8 arcsec (7 kpc). Mg II emission has been spatially resolved in at least two individual galaxies. Rubin et al. (2011) found that Mg II emission from a $z = 0.69$ galaxy extended to radii of ≥6.5 kpc; the mass outflow rate estimated by Martin et al. (2013) of 35–40 M$_\odot$ yr^{-1} is about half the SFR. For a $z = 0.93$ galaxy, Martin et al. (2013) found Mg II emission extending out to 11 kpc; this Mg II emission shows different spatial distribution and kinematics than the [O II] emission, indicating that the Mg II is scattered rather than coming directly from the H II regions. They inferred a mass flux of 330–500 M$_\odot$ yr^{-1}, which is 4–6 times larger than the SFR. Martin et al. (2013) caution that this galaxy is exceptional in their sample: of the 145 galaxy spectra from Martin et al. (2012) that covered the Mg II doublet and Fe II absorption, 22 showed strong Mg II emission, but for only three galaxies was the emission clearly spatially resolved.

Fe II fine-structure emission is generally not seen in local star-forming and starburst galaxies (Leitherer et al. 2011). However, both Fe II and Mg II emission features are seen at higher redshift star-forming galaxies. Some authors have argued that if Mg II emission typically occurs on large spatial scales, compared to the stellar continuum, then slit losses may explain why Mg II emission is rarely seen in observations of $z \sim 0$ galaxies; as the slits used to observe such objects are generally placed to cover only the central regions of the galaxies and capture little emission from the spatially extended outflows (Giavalisco et al. 2011; Erb et al. 2012). Prochaska, Kasen & Rubin (2011) modelled this effects of slit loss, finding in their models that the emission is sufficiently centrally concentrated, and the emission-to-absorption ratio is unaffected for slit widths that cover more than 4–5 kpc of the galaxies.

The limited spatial resolution typical of observations of Mg II and Fe II emission translates to as-yet unsatisfying constraints on the location, maximum velocity, and total column density of the warm outflowing gas. Absorbing clouds may lie anywhere along the line of sight to the galaxy, and the decline in gas covering fraction with increasing blueshift makes it challenging to detect the highest velocity gas (Martin & Bouché 2009). Gravitationally lensed galaxies provide access to smaller spatial scales, and higher signal-to-noise (S/N) ratios, than are possible for field galaxies. One approach would be to map the outflows via Mg II and Fe II emission using large-format integral field spectrographs like MUSE on the VLT. Such an approach would cover both large spatial scales (from the large format of the IFU) as well as sub-kiloparsec scales (accessible through lensing magnification).

Another approach, employed in this paper, is to examine the kinematics of the outflow at multiple positions within a lensed galaxy, and examine how the properties of the outflow may depend on the properties of the star-forming complexes that ultimately should drive the outflow. In this work, we perform the first spatially resolved down-the-barrel study of galactic outflows using the lensed, $z = 1.7$ spatially resolved galaxy RCSGA 032727-132609 as the background source (Wuyts et al. 2010). We observe the Mg II and Fe II absorption and emission lines for four spatially resolved star-forming knots in this galaxy. These knots are physically separated by 2–6 kpc (Wuyts et al. 2014). As such, this work probes smaller spatial scales, with more detailed kinematics, than have been accessed previously with observations of field galaxies. We compare the outflow absorption and emission strength and kinematics to the properties of the star-forming regions, namely SFR and stellar masses estimated from *Hubble Space Telescope* (*HST*)/WFC3 photometry and grism spectra.

The paper is organized as follows. In Section 2, we describe the observations and the methods used to estimate the properties of these star-forming knots. In Section 3, we describe the method used to estimate the outflowing absorption and emission gas properties. In Sections 4.1 and 4.2, we compare the estimated outflowing absorption and emission strength and kinematics with the properties of the star-forming knots. In Section 4.3, we study the pixel velocity distribution of the outflowing gas. In Section 4.4, we estimate the spatial extent of the Mg II emission region. In Section 4.5, we estimate the minimum mass outflow rates in each individual knot. In Section 4.6, we compare our findings with the outflow properties observed in local starburst galaxies. In Section 5, we summarize our findings.

Throughout this paper, we assume a cosmology of $\Omega_m = 0.3$, $\Omega_\Lambda = 0.7$, $H_0 = 70$ km s^{-1} Mpc^{-1}, and $h \equiv H_0/100 = 0.7$. Solar abundances are taken from table 1 of Asplund et al. (2009). The initial mass function (IMF) is Chabrier (2003).

2 METHODS

2.1 Observations

The lensed galaxy RCSGA 032727-132609, hereafter RCS0327, is lensed by the galaxy cluster RCS2 032727-132623. It was discovered in the Second Red Sequence Cluster Survey (Gilbank et al. 2011); the discovery paper is Wuyts et al. (2010). Images obtained

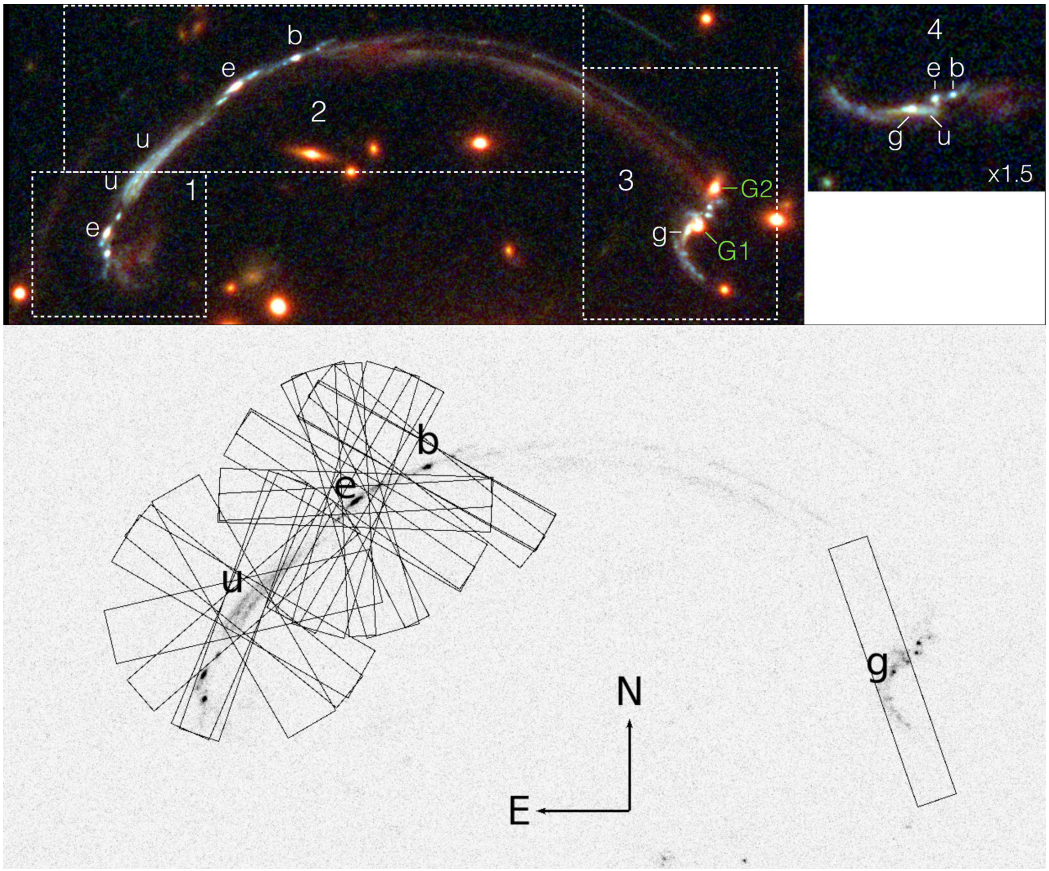

Figure 1. Lensed galaxy RCSGA 032727-132609. TOP: colour rendition composed of *HST*/WFC3 F160W, F125W, F098M (red); F814W, F606W (green); and F390W (blue). The dashed lines approximately mark the multiple images, indicated by numbers. The emission knots with MagE spectroscopy are labelled as 'e', 'u', 'b', and 'g'. Two cluster galaxies 'G1' and 'G2' are in image 3. The right-hand panel shows a zoomed-in view of the counter-image, which is a relatively undistorted image of the source-plane galaxy. Figure adapted from Sharon et al. (2012). BOTTOM: *HST*/WFC3 F390W image, with MagE observations overplotted. One slit is drawn for each integration, using our best estimate of the pointing, the actual slit position angle, and the slit width used during that observation. Since the slit was regularly rotated to track the parallactic angle, Knots U and E were observed using a wide range of slit position angles. The length of the MagE slit is a fixed 10 arcsec. North is up and east is left.

with the *HST* (Programme 12267, PI Rigby) have enabled a high-fidelity lensing model and source-plane reconstruction (Sharon et al. 2012, see their fig. 4). We adopt this lensing model. Fig. 1 of Sharon et al. (2012) named the regions within RCS0327; we adopt this nomenclature, but capitalize the named regions for readability.

Rest-ultraviolet spectra of RCS0327 were obtained using the MagE spectrograph (Marshall et al. 2008) on the 6.5 m Magellan II telescope at Las Campanas Observatory in Chile. Observations, mostly at low airmass (sec(z)< 1.4), were obtained in the course of seven nights from 2008 to 2013. The atmospheric seeing, as measured by the guide camera during observations, was sub-arcsecond for all observations. The observations are part of a larger survey of the rest-ultraviolet spectra of bright lensed galaxies; a future paper will present the full spectra and complete details of the observations for the full sample (Rigby et al., in preparation).

To summarize the MagE observations of RCS0327 for the purposes of this paper, three different slits were used, all 10 arcsec length, with the following widths:

(i) 2 arcsec wide, with resolution $R = 2050$ (145 km s^{-1} per resolution element);
(ii) 1.5 arcsec wide, with $R = 2730$ (108 km s^{-1});
(iii) 1 arcsec wide, with $R = 4100$ (72 km s^{-1}).

No detector binning was used. The slit position angle was updated hourly to keep it close to the parallactic angle, thus preserving relative fluxing of the spectrum; this is especially important given the wide wavelength coverage of MagE. For a few integrations, a non-parallactic slit position was chosen to keep potentially contaminating objects out of the slit.

Since the RCS0327 arc at 38 arcsec is much longer than the 10 arcsec MagE slit, we could not target the entire arc. Instead we targeted four physically distinct bright physical regions within RCS0327: Knots B, E, G, and U. Fig. 1 shows how the MagE slit was positioned in the image plane. The total integration time was 10.00 h on Knot E, 7.94 h on Knot U, 2.83 h on Knot B, and 1.83 h on Knot G. Table 1 tabulates the effective spectral resolution for each knot spectrum weighted by the integration time. Fig. 1 shows that in the image plane, Knots U, E, B, and G are separated from each other by more than 2 arcsec. Given the sub-arcsecond seeing conditions during the observations, and the slit position angles shown in Fig. 1, we expect minimal cross-contamination of each slit by emission from adjacent regions.

2.2 Calibration and data reduction

Full details of the calibration and reduction of the MagE data will be given in the MagE sample paper (Rigby et al., in

Table 1. The physical properties of the individual knots of RCS0327. Nebular redshifts from the Hα emission line, from the following references: (1) the Keck/NIRSPEC spectra of Rigby et al. (2011) re-analysed by Wuyts et al. (2014); and (2) the Keck/OSIRIS spectra of Wuyts et al. (2014). For convenience, the last column gives the velocity offset with respect to Knot E. SFR is measured from H β luminosity, following Kennicutt (1998), assuming a Chabrier IMF, corrected for extinction and outflows, and demagnified for lensing. The associated uncertainty is the standard deviation when images of multiple knots could be measured. Otherwise the uncertainty quoted is the statistical uncertainty, which mostly comes from the line flux uncertainty.

Properties of the individual knots of RCS0327							
Knot	$\log M^*/M_\odot$	SFR ($M_\odot$ yr^{-1})	Σ_{SFR} ($M_\odot$ yr^{-1} kpc^{-2})	$z_{sys} \pm z_{error}$	FWHM (km s^{-1})	Instrument	Offset (km s^{-1})
Knot E	$8.5^{+0.1}_{-0.4}$	14 ± 0.4	1.87 ± 0.06	$1.703\,7455 \pm 0.000005$	109	NIRSPEC	0
Knot U[1]	7.5[1]	1.1 ± 0.1	1.54 ± 0.24	$1.703\,8840 \pm 0.000007$	128	NIRSPEC	15
Knot B	$7.7^{+0.5}_{-0.2}$	10 ± 0.4	1.14 ± 0.28	$1.703\,6000 \pm 0.000070$	109	OSIRIS	−16
Knot G	$8.7^{+0.5}_{-0.1}$	65 ± 3.0	2.33 ± 0.11	$1.703\,8500 \pm 0.000050$	108	OSIRIS	12

Note. [1] The magnification of Knot U is extremely high and therefore extremely uncertain. This uncertainty is not fully captured by the error bar.

preparation). To summarize, wavelength calibration was accomplished by internal thorium argon lamp spectra, obtained at each pointing of the telescope, to guard against instrument flexure. Flat-fielding was accomplished using an internal Xe lamp for the blue orders, and a quartz lamp for the redder orders. The MagE spectra for each night were reduced separately using the Las Campanas Observatory (LCO) MagE pipeline written by D. Kelson. The spectra for each night were then fluxed using spectrophotometric standard stars observed nightly. Overlapping orders were combined with a weighted average, which was then corrected to vacuum barycentric wavelength. Telluric absorption, particularly the *A* band of molecular absorption at 7590–7660 Å (Wark & Mercer 1965), was corrected using the featureless standard star EG 131 and the IRAF task *noao.onedspec.telluric*. Since the *A* band begins 10 Å redward of the reddest part of the Mg II doublet in RCS0327, the telluric correction is largely cosmetic and does not affect the results presented here. For each knot, spectra from multiple nights were then combined with a weighted average.

2.3 Knot properties

Knots B, D, E, F, G, and U of RCS0327 have complementary rest-frame optical (observed-frame near-infrared) spectra from NIRSPEC on the Keck II telescope and OSIRIS on Keck II (Rigby et al. 2011; Wuyts et al. 2014). We list the redshifts of these knots in Table 1, derived from H α in the NIRSPEC or OSIRIS spectra.

Multiple measurements exist for the SFR of the RCS0327 knots. We choose not to use the H α measurements due to challenges of flux calibration across multiple telescopes, instruments with different slit widths, and variation in seeing conditions. Instead, we take as our SFR indicator, the extinction-corrected H β luminosity, as measured by the WFC3 G141 grism and published in Whitaker et al. (2014). For the extinction, we use $E(B-V) = 0.4$, which was found by Whitaker et al. (2014) to be the reddening that best fit the H β/H γ ratio in the grism spectra, and the conversion from reddening to extinction of $R = 4.05$ (Calzetti, Kinney & Storchi-Bergmann 1994). We correct the H β flux for the outflow component, which contributes 0–50 per cent of the total H α line flux, as measured by Wuyts et al. (2014) from the velocity profile of H α. These outflow fractions are taken from column 7 of table 3 of Wuyts et al. 2014. To convert from H β luminosity to SFR, we use equation 2 of Kennicutt (1998), modified to use the Chabrier IMF (Chabrier 2003), and an H α to H β flux ratio of 2.863 which is true for Case B, $T = 10^4$ K, $n = 100$ cm^{-3}.

When grism H β measurements are available for multiple lensed images of the same knot, we quote the weighted mean and the error in the weighted mean. For cases with only one measurement, we quote the statistical uncertainty, which mostly comes from the line flux uncertainty, and ignores the magnification uncertainty which probably dominates. These derived SFR are tabulated in Table 1. Stellar masses for each knot were measured by spectral energy distribution (SED) fitting, as described in Wuyts et al. (2014). SED fitting is highly uncertain for Knot U because it sits on the caustic and therefore has an extremely high magnification whose value is quite uncertain, as well as a highly distorted appearance in the image plane that complicates aperture photometry. Therefore, to derive an approximate stellar mass for Knot U, we assume that the Knots E and U have the same mass-to-light ratio, and scale their H β fluxes, resulting in an estimated stellar mass for Knot U of $\log M^* = 7.5\,M_\odot$.

We estimate the halo mass of the galaxy from mock catalogues generated from the Bolshoi simulation (Klypin, Trujillo-Gomez & Primack 2011). Haloes were found using ROCKSTAR halo finder (Behroozi, Wechsler & Wu 2013). RCS0327 is a merger with stellar masses of the two merging galaxies being 5.1×10^9 and $1.2 \times 10^9\,M_\odot$, respectively (Wuyts et al. 2014). We search for galaxy pairs in the mocks with similar stellar masses and physical separations <100 kpc from each other. This gives us a distribution of halo masses for the higher mass galaxy and we adopt the mean halo mass as the halo mass of the system. Thus we assign a halo mass for the galaxy as $\log M_{halo} = 11.6 \pm 0.3\ M_\odot$, the maximum circular velocity $v_{circ} = 156 \pm 28$ km s^{-1}. For a halo with outer radius r_h, the escape velocity at radius R (for a flat rotation curve), is given as $v^2_{esc}(R) = 2v^2_{circ} \ln(1 + r_h/R)$ (Binney & Tremaine 1987). The escape velocities (v_{esc}) for this galaxy at $R = 5$, 20 and 50 kpc are given as 411 ± 74, 324 ± 59 and 262 ± 48 km s^{-1}, respectively.

3 MODELLING THE OBSERVED Mg II AND Fe II LINE PROFILES

In this section, we describe the models used to characterize the observed Mg II and Fe II doublets. The transitions used in this work are listed in Table 2. We use these models to quantify the mean blueshifted absorption and redshifted emission profiles. We first describe the model used to characterize the Mg II doublet. We quantify the absorption due to the interstellar medium (ISM) of the host

Table 2. Mg II and Fe II transitions studied. [a]Vacuum wavelengths from Morton (2003). [b]Orbital angular momenta. [c]Einstein *A*-coefficients.

Mg II and Fe II transitions studied					
Transition	λ^a (Å)	$J^b_{\rm high}$	$J^b_{\rm low}$	A^c (s^{-1})	Feature
Mg II	2796.351	3/2	0	2.63E+08	Resonant abs/em
	2803.528	1/2	0	2.60E+08	Resonant abs/em
Fe II	2600.173	9/2	9/2	2.36E+08	Resonant abs
	2586.650	7/2	9/2	8.61E+07	Resonant abs
	2626.451	9/2	7/2	3.41E+07	Fine-structure em
	2612.654	7/2	7/2	1.23E+07	Fine-structure em

galaxy as the systemic ISM absorption component and model the outflowing and inflowing gas. The outflowing gas moving away from the galaxy will absorb photons at blueshifted (negative) velocities with respect to the systemic redshift of the galaxy and the inflowing gas will move towards the galaxy and will absorb photons at redshifted (positive) velocities. This outflowing gas could have some velocity dispersion (generally much lower than the thermal broadening of individual clouds) and even complex kinematic structures. However, due to moderate resolution of the spectra, such kinematic complexities can be neglected. The systemic redshift for each knot was obtained from H α emission lines in NIRSPEC or OSIRIS spectra and are tabulated in Table 1. The model that describes the systemic ISM component of the Mg II and Fe II absorption, centred on the systemic redshift of the galaxy is

$$1 - A_{\rm sys}(\lambda) \; = \; 1 - (\tau_1 G(v, b, \lambda_1) + \tau_2 G(v, b, \lambda_2)); \qquad (1)$$

where τ_1 and τ_2 are the optical depths at the centre of the absorption profiles given by two Gaussians, $G(v, b, \lambda_1)$ and $G(v, b, \lambda_2)$. These Gaussians are centred at the systemic zero velocity of the galaxy and have a velocity width given by b. For the systemic component, the individual absorption lines are likely to be optically thick as they are accounting for both the Galactic ISM as well as absorption from stellar atmospheres. Therefore we assume a doublet ratio of 1 ($\tau_1 = \tau_2$) for all the systemic components. The final model for the observed absorption and emission line profile is given as

$$F_{\rm model}(\lambda) = F_{\rm c}(\lambda)[1 - A_{\rm sys}(\lambda)][1 - A_{\rm outflow}(\lambda)] \\ [1 - A_{\rm inflow}(\lambda)][1 + F_{\rm em}(\lambda)]; \qquad (2)$$

where $F_{\rm model}(\lambda)$ is the model flux density, $F_{\rm c}(\lambda)$ is the continuum level, $[1 - A_{\rm sys}(\lambda)]$ is the systemic ISM absorption component, $[1 - A_{\rm outflow}(\lambda)]$ is the blueshifted outflowing gas, $[1 - A_{\rm inflow}(\lambda)]$ is the redshifted inflowing gas and $[1 + F_{\rm em}(\lambda)]$ is the emission component. All the absorption components in the inflowing and outflowing models are taken to be the sum of two Gaussians centred at the rest-frame wavelength of each component of the doublet similar to equation 1. For the outflowing and inflowing components, we allow the doublet ratio to vary from 1 to 2 and the velocity centroids of the Gaussians are allowed to vary to represent outflowing or inflowing gas.

For the Mg II transition, we model the resonant emission lines with two Gaussians and allow their centres to vary to match the observed emission lines. Similarly, we model the Fe II 2612 and Fe II 2626 fluorescent emission lines with two Gaussians. Finally, before comparing the model spectrum to the data, we convolve $F_{\rm model}(\lambda)$ with a Gaussian having an full width at half-maximum (FWHM) equal to the velocity resolution of each spectrum (Table 1). This gives the final model spectrum $F_{\rm obs}(\lambda)$, which we compare to the data. Because the instrumental resolution is comparable to the expected flow velocities and widths (with FWHMs ranging between ∼108 and 128 km s^{-1}), this step significantly changes the shape of $F_{\rm model}(\lambda)$, and this step is crucial to estimating robust model parameter constraints. There are four free parameters for each component: Doppler shift of the lines, optical depth at line centre, Doppler width and doublet ratio. There are four independent model components: systemic, inflowing, outflowing and emission. This gives a total of 15 free parameters (the doublet ratio for the systemic component is fixed at 1). Because of the moderate spectral resolution and finite S/N of the individual spectrum, the Doppler shift and the optical depths are the best constrained and we will not discuss the other parameters in detail.

To constrain the best fitting model parameters from the data, we developed a customized code in IDL, which samples the posterior probability density function (PPDF) for each model using the adaptive multiple chain Markov Chain Monte Carlo (MCMC) technique (Haario, Saksman & Tamminen 2001). Fig. 2 top panel and Fig. 3 shows the best-fitting model profiles along with the observed spectra. We adopt a uniform prior over the allowed parameter intervals, adjusting slightly these intervals for each model and transition. Our code produces the marginalized PPDFs for each of the fitted parameters. We require each PPDF to be populated with 50 000 realizations, and we visually inspect the PPDFs for each fit to check that the MCMC chains have converged.

For each realization, we compute the rest-frame equivalent width of each model component given as $W = \int(1 - \tau_1 G_1(\lambda))d\lambda$. This quantity is computed for both Mg II and Fe II outflow absorption and emission profiles. This yields a distribution of W measurements; we take the mode of the W distribution as the rest-frame equivalent width for that transition, and the ± 34th percentile W around the mode as the lower and upper bounds on the uncertainty on the W measurements, respectively. Similarly we estimate the absorption weighted outflow velocity for each transition in each realization given as $\bar{v} = \int v(1 - \tau_1 G_1(v))dv$. We take the mode of the velocity distribution to parametrize the velocity for that transition and the ± 34th percentile velocities around the mode as the lower and upper bounds on the uncertainty on velocity, respectively. For any absorption at the rest-frame wavelength $\lambda_{\rm rest}$, with an oscillator strength f_0, the estimated column density is given as

$$N\ [{\rm cm}^{-2}] \; = \; \frac{\tau_0 b_D\ [{\rm km\ s}^{-1}]}{1.497 \times 10^{-15} \lambda_{\rm rest}\ [\text{Å}] f_0}; \qquad (3)$$

where τ_0 is the optical depth at the centre of the absorption line and b_D is the fitted Doppler width of the absorption line (where $b_D = \sqrt{2}b$).

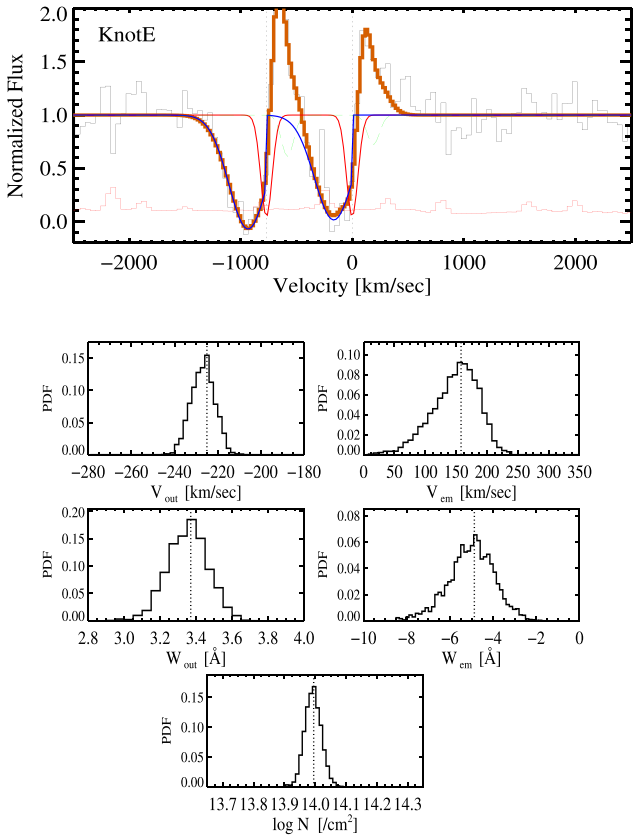

Figure 2. Top: observations of Mg II 2796, 2803 transitions with the model fits for Knot E. The black stairs represent the observer spectra and the red stairs represent the error spectra. The brown lines show the best-fitting model profile to the data, after convolving with the instrumental spread function. The blue lines show the outflowing components, and the red smooth line shows the systemic component. The dashed green line represents the inflowing component, which is very small. Lower panels: The marginalized PPDFs for the outflow velocity (V_{out}), emission velocity (V_{em}), rest-frame outflow absorption equivalent width (W_{out}), rest-frame emission equivalent width (W_{em}) and Mg II column density estimate (log N), respectively. The vertical dashed lines show the mode of the distributions which are taken as the best model estimates for each case, respectively.

The top panel of Fig. 2 shows the best-fitting Mg II model F_{model} (solid brown line) with the observed the Mg II 2796, 2803 doublet for Knot E. The lower panels show the marginalized PPDFs for the estimated outflow velocity (V_{out}), emission velocity (V_{em}), outflow absorption equivalent width (W_{out}), emission equivalent width (W_{em}) and Mg II column density estimate (log N), respectively. For the Mg II 2796, 2803 transition in Knot E, we estimate the outflow velocity (V_{out}) $= -225^{+4}_{-7}$ (km s^{-1}), outflow absorption equivalent width (W_{out}) $= 3.37^{+0.10}_{-0.13}$ Å, outflow emission velocity (V_{em}) $= 158^{+27}_{-48}$ (km s^{-1}), outflow emission equivalent width (W_{em}) $= -4.87^{+0.87}_{-1.18}$ Å, and outflow Mg II column density (log N/cm^{-2}) $= 14^{+0.02}_{-0.0.03}$, respectively. These measurements for all four knots are listed in Table 3.

4 RESULTS

In the following section, we discuss the variation of emission/absorption strengths and kinematics of gas traced by Mg II and Fe II emission and absorption lines relative to their systemic redshift of the galaxy RCS0327. We also discuss the variation of outflow absorption and emission properties with the physical properties (stellar mass, SFR, specific SFR) of the individual knots.

4.1 Dependence with mass and SFR

4.1.1 Fe II emission

We first focus on the emission strengths and kinematics of the Fe II transitions. The Fe II ion exhibits a complex and large set of transitions in the rest-frame ultraviolet wavelength range. The Fe^{+} transition alone is found to be associated with at least millions of recorded energy levels (Kurucz 2005). The Fe II resonant absorption lines have been extensively used to study galactic outflows, as it redshifts into the optical wavelength range at high redshifts (Coil et al. 2011; Kornei et al. 2012, 2013; Martin et al. 2012; Rubin et al. 2012). The absorption of a single resonant photon by Fe^{+} can lead to either re-emission of another resonant photon to the ground state following an electronic transition to the ground state (resonant emission) or the emission of a photon to an excited ground state (fluorescence emission). In our data, we observe the Fe II 2586, 2600 resonant absorption doublet, but we do not observe resonant Fe II emission. We further observe fluorescence Fe II emission at 2612 and 2626 Å, respectively. The absence of Fe II 2586, 2600 resonant emission is due to multiple scattering of the photons re-emitted with the resonant energy, as they interact with the same ions in the wind where they were created (see Scarlata & Panagia 2015 for a detailed discussion). Such multiple scatterings will not change the shape of the absorption profile but will suppress the contribution of the re-emission in the resonant emission line, while simultaneously enhancing the re-emission strength in the florescence channel (Scarlata & Panagia 2015). In case of Mg II 2796, 2803 transition, the florescence channel is absent. Because of that, the multiple scattering of photons do not change the Mg II resonant emission profile and we observe the Mg II resonant emission lines but not the Fe II 2586, 2600 resonant emission lines (see Fig. 3).

Fig. 4 shows how Fe II 2612, 2626 emission velocities and emission equivalent widths vary with the physical properties of the knots. The top row shows the variation with the stellar mass of the knots, the middle row shows the variation with SFR and the last panel shows the variation with the sSFR of these knots. We find that the Fe II emission velocity centroids (blue and grey squares) are more consistent with either being blueshifted or close to being at the systemic zero velocity of the individual knots. The mean velocity of the four individual measurements for Fe II 2612 emission line is -20 ± 29 km s^{-1}, and Fe II 2626 line is -28 ± 3 km s^{-1}, respectively. We find no detectable correlation of Fe II emission velocities with stellar mass, SFR or sSFR of the individual knots.

This absence of a kinematic shift relative to the systemic velocities does not necessarily imply that the associated gas is at rest with respect to the stars of the galaxy. Simple radiative transfer models for outflowing gas predict the net Fe II emission velocities to be close to the systemic zero velocity of the host galaxy for an optically thin wind (Prochaska et al. 2011). Such a model will transmit the scattered Fe II emission photons from both backside and frontside of the wind. Further, if the dust opacity increases, the Fe II emission velocities will be slightly blueshifted, because the redshifted photons scattering off the backside of the wind will be absorbed preferentially, due to the longer path lengths. This scenario is consistent with the measurements given in Fig. 4.

Looking at the Fe II 2612, 2626 emission equivalent widths, we see that knots with lower SFRs exhibit higher emission equivalent

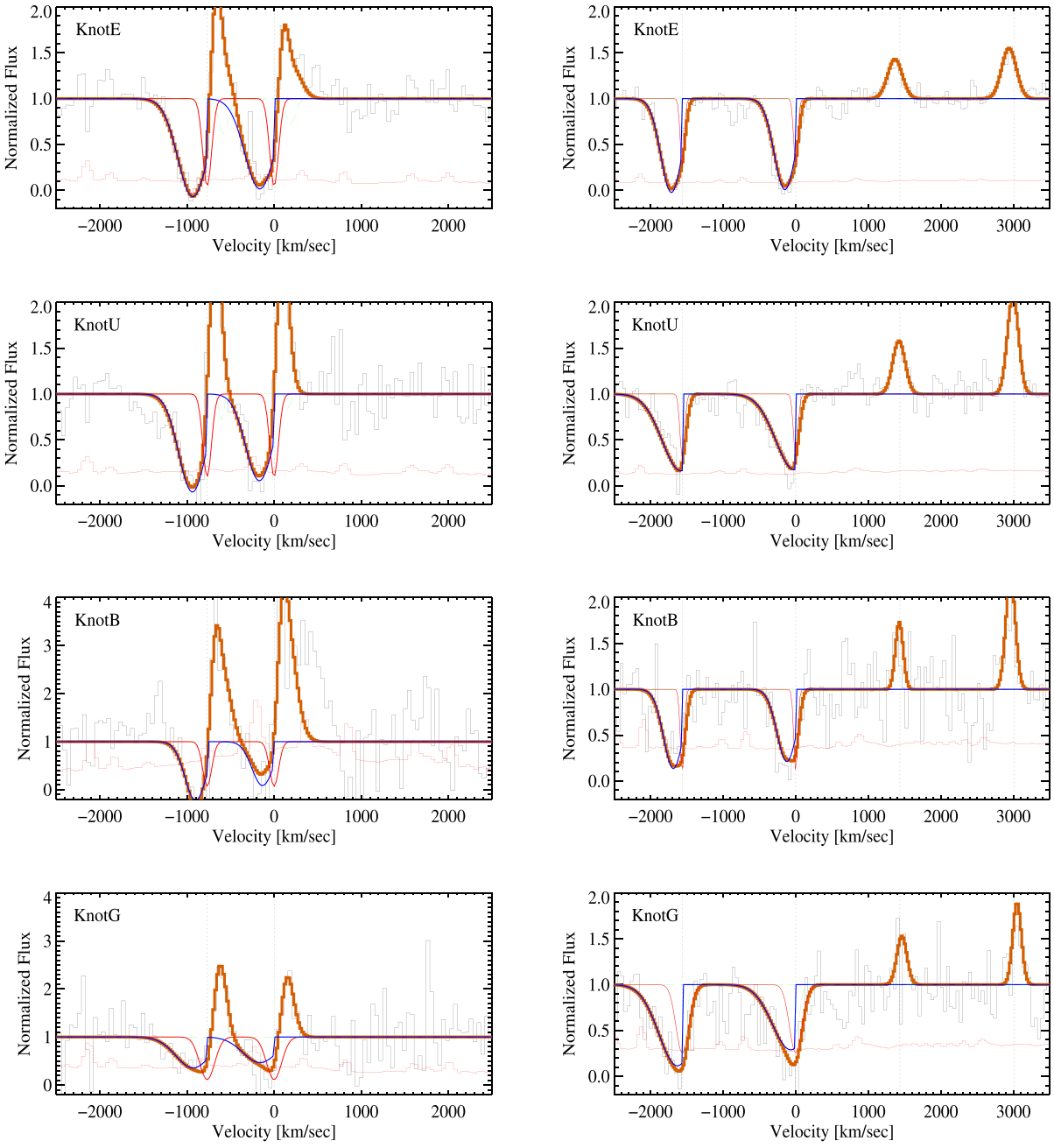

Figure 3. Mg II and Fe II outflow profiles with fits. The black stairs represent the observer spectra and the red stairs represent the error spectra. The brown lines show the best-fitting model profile to the data, after convolving with the instrumental spread function. The blue lines show the outflowing components, and the red smooth line shows the systemic component. The dashed green line represents the inflowing component, which is very small. Knot B and Knot G were re-binned with 2 pixel windows for presentation purposes.

widths. A Pearson linear correlation test for the combined Fe II 2612, 2626 line equivalent widths show a 2.9σ inverse correlation with log SFR of the individual knots. This result is consistent with Erb et al. (2012) and Kornei et al. (2013), where amongst their Fe II emission line showing galaxies, the strongest Fe II emission lines were observed in the galaxies with smaller stellar masses and lower SFR. We do not detect any statistically significant correlation of Fe II emission line strength with stellar mass or specific SFR of the individual knots.

4.1.2 Mg II emission

We now focus on the emission kinematics and strength of the Mg II doublet transition. The strong resonant Mg II absorption doublet transition is easily identifiable and extensively used as a tracer of galactic winds (e.g. Weiner et al. 2009; Rubin et al. 2010; Martin et al. 2012; Bordoloi et al. 2014b). While the Mg II doublet is primarily seen in absorption, it is also seen with a P-Cygni emission profile in a wide variety of objects. The P-Cygni Mg II emission profile has been seen in Seyferts (Wu, Boggess & Gull 1983), Ultra-Luminous

Table 3. The measured Mg II and Fe II outflow kinematics, equivalent widths and column densities as well as the Mg II resonant emission and Fe II 2612, 2626 fluorescence emission kinematics and strengths.

Transition	Measurement	Measured absorption and emission kinematics and strengths of the individual knots of RCS0327 Knot E	Knot U	Knot B	Knot G
Mg II	V_{out}(km s^{-1})	-225^{+4}_{-7}	-233^{+10}_{-7}	-183^{+16}_{-20}	-251^{+33}_{-33}
Mg II	W_{out}/(Å)	$3.37^{+0.10}_{-0.13}$	$3.27^{+0.14}_{-0.16}$	$2.41^{+0.25}_{-0.46}$	$2.03^{+0.44}_{-0.54}$
Mg II	log N/(cm^{-2})	$14^{+0.02}_{-0.0.03}$	$14.16^{+0.03}_{-0.03}$	$13.9^{+0.11}_{-0.08}$	$13.9^{+0.12}_{-0.20}$
Mg II	V_{em}(km s^{-1})	158^{+27}_{-48}	70^{+9}_{-14}	208^{+18}_{-93}	155^{+7}_{-36}
Mg II	W_{em}/(Å)	$-4.87^{+0.87}_{-1.18}$	$-5.96^{+0.43}_{-0.95}$	$-11.19^{+2.32}_{-2.14}$	$-3.05^{+0.91}_{-1.53}$
Fe II	V_{out}(km s^{-1})	-195^{+3}_{-4}	-222^{+14}_{-13}	-171^{+20}_{-20}	-235^{+30}_{-39}
Fe II	W_{out}/(Å)	$2.63^{+0.05}_{-0.07}$	$2.38^{+0.09}_{-0.13}$	$1.86^{+0.18}_{-0.37}$	$2.32^{+0.23}_{-0.44}$
Fe II	log N/(cm^{-2})	$14.34^{+0.02}_{-0.02}$	$14.52^{+0.02}_{-0.04}$	$14.23^{+0.12}_{-0.14}$	$14.42^{+0.11}_{-0.10}$
Fe II 2612	V_{em}(km s^{-1})	-66^{+12}_{-16}	-14^{+15}_{-12}	-60^{+32}_{-18}	61^{+25}_{-89}
Fe II 2612	W_{em}/(Å)	$-0.95^{+0.09}_{-0.08}$	$-1.02^{+0.14}_{-0.13}$	$-0.63^{+0.23}_{-0.26}$	$-0.63^{+0.28}_{-0.30}$
Fe II 2626	V_{em}(km s^{-1})	-30^{+5}_{-5}	-22^{+7}_{-5}	-29^{+15}_{-15}	-30^{+28}_{-16}
Fe II 2626	W_{em}/(Å)	$-1.17^{+0.08}_{-0.10}$	$-1.77^{+0.15}_{-0.13}$	$-1.19^{+0.20}_{-0.38}$	$-0.80^{+0.19}_{-0.28}$

Infrared galaxies (Martin & Bouché 2009), local star-forming galaxies (Kinney et al. 1993), high-redshift star-forming galaxies (Weiner et al. 2009; Rubin et al. 2010; Bordoloi et al. 2014b) etc. The most viable hypothesis for the physical origin of Mg II emission doublet is photons scattering off the backside of galactic winds (Prochaska et al. 2011). This process has also been observed for Lyα emission in LBGs (Pettini et al. 2001). Both Mg II absorption lines can be strongly affected by resonant emission filling, as there are no excited ground states available for fluorescence.

Fig. 4 shows how Mg II emission velocities and emission equivalent widths vary with the physical properties of the knots. The Mg II emission equivalent widths show a weak trend with SFR of the individual clumps. The Mg II emission velocities (red diamonds) are always redshifted with respect to the systemic redshift of the host star-forming knots. The mean Mg II emission line velocity for the four knots is 148 $\pm$ 29 km s^{-1}. This finding with local star-forming knots is consistent with the other studies looking at global galaxy properties, where it was found that the typical Mg II emission velocities are $\approx$100 km s^{-1} redward of the systemic redshift of the galaxies (Weiner et al. 2009; Kornei et al. 2013; Rubin et al. 2014). Resonant Mg II emission lines are not ubiquitously seen in down-the-barrel galaxy spectra: Kornei et al. (2013) reported that they detect Mg II emission in 15 per cent of their galaxies showing blueshifted Mg II absorption. Erb et al. (2012) studying a higher resolution sample reported the detection rate of Mg II emission in 30 per cent of their sample. Erb et al. (2012) found that Mg II emitters are typically drawn from bluer, higher star-forming galaxies. This might be owing to a combination of their lower resolution spectra and Mg II emission filling, making detection of any weak emission difficult.

4.1.3 *Outflows traced by Mg II and Fe II*

In this section, we study the outflow gas kinematics and absorption strengths traced by Mg II and Fe II resonant transitions. Fig. 5 shows the variation of Mg II and Fe II outflow velocities and equivalent widths with stellar mass, SFR and sSFR of the individual knots. The outflow velocities traced by Mg II and Fe II transitions are very similar, but the blueshifted outflow velocities traced by Mg II absorption are systematically higher compared to that traced by Fe II absorption by an average of $\sim$17 $\pm$ 5 km s^{-1}. We believe this small offset is due to our inability to completely account for emission filling by resonant Mg II emission. However, the good agreement between the Fe II and Mg II traced outflow velocity estimates suggest that our model of Mg II emission is doing a reasonably good job in reproducing the total Mg II emission in these galaxies.

The mean outflow velocities as traced by both Fe II and Mg II absorption are different from one knot to the other, after accounting for measurement uncertainties. The mean Mg II traced outflow velocity for the four knots is -223 ± 14 km s^{-1}, and the individual outflow velocities vary from -251 km s^{-1} to -183 km s^{-1}. Similarly, the mean Fe II-traced outflow velocity for the four knots is -206 ± 15 km s^{-1}, and the individual outflow velocities vary from -235 km s^{-1} to -170 km s^{-1}. Hence, for both independent tracers, we see a maximum velocity difference $\approx$ 70 km s^{-1} between individual knots. This variation is significantly larger than the differences in nebular redshift of the knots, which only differ by $\sim$ 15 km s^{-1} (see Table 1).

The outflow velocities show weak trends with SFR and stellar mass of the individual knots, but these trends are not statistically significant (Fig. 5). The outflow velocities measured for individual star-forming knots are similar to the average outflow velocities observed for whole galaxies by Weiner et al. (2009) and Bordoloi et al. (2014b) in their analysis of stacked down-the-barrel galaxy spectra.

4.2 Dependence with Σ_{SFR}

In this section, we discuss how outflow properties and emission properties depend on the SFR surface density (Σ_{SFR}). We estimate Σ_{SFR} for each knot self-consistently, using the extinction-corrected SFRs from the *HST* grism observations, and the apertures used to extract those spectra. Σ_{SFR} is the demagnified SFR divided by the demagnified area of the aperture in the source plane. We employ this method so that the magnification used to compute the intrinsic SFR is the same magnification used to compute the area of the aperture in the source plane.

4.2.1 *Fe II and Mg II emission*

In Fig. 6, the top panels show the variation of Mg II and Fe II emission velocities and emission equivalent widths as a function of Σ_{SFR}. The

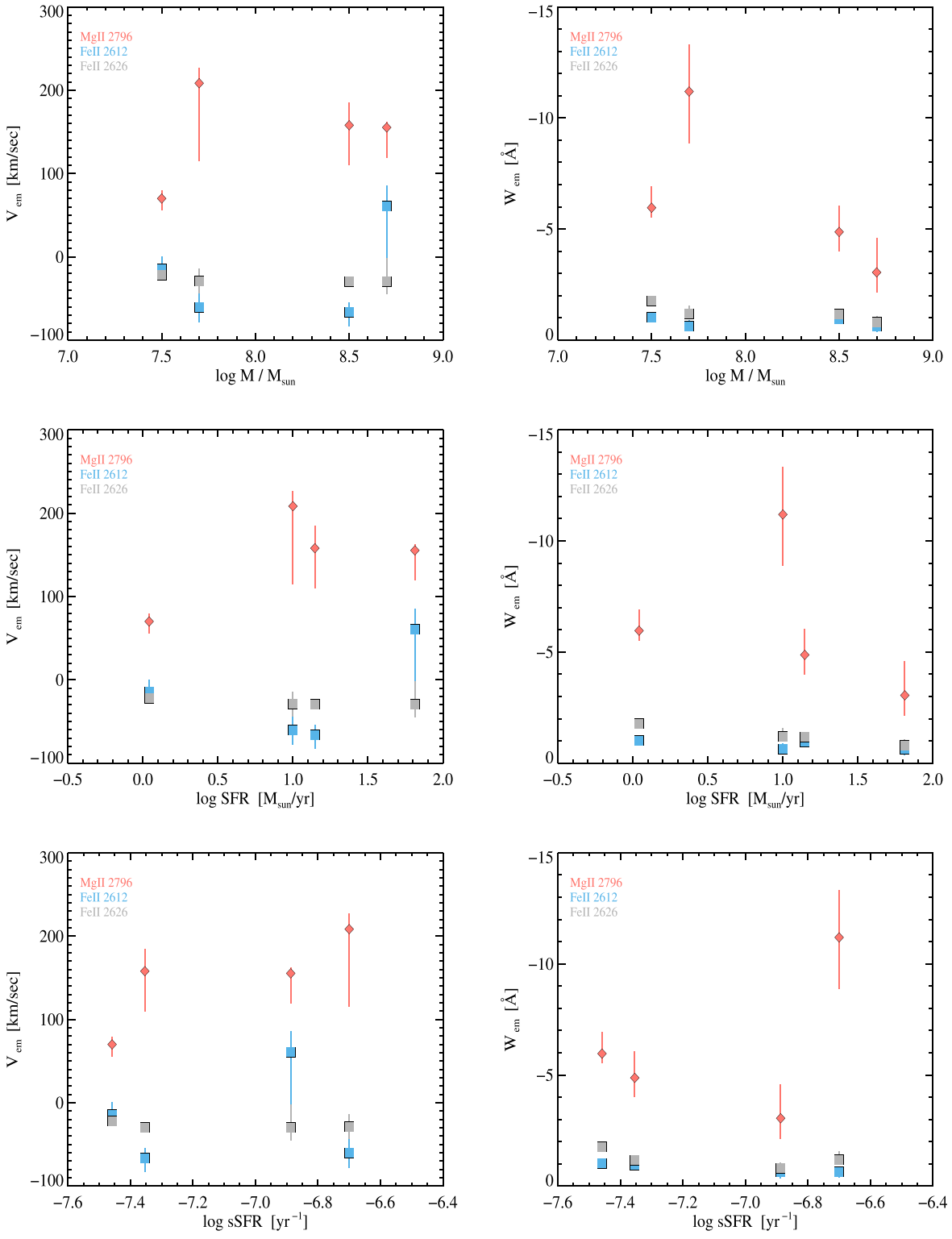

Figure 4. Variation of Mg II and Fe II emission kinematics (left-hand panels) and equivalent widths (right-hand panels) as a function of stellar mass (top panels), SFR (middle panels) and sSFR (bottom panels) of the individual knots, respectively. Mg II resonant emission (red diamonds) lines are always redshifted relative to the systemic zero velocity of the knots, whereas the fluorescent Fe II 2612 (blue squares) and Fe II 2626 (grey squares) emission lines are consistent with being at the systemic zero velocity of the knots. Fe II emission equivalent widths increase with decreasing SFR in the individual knots.

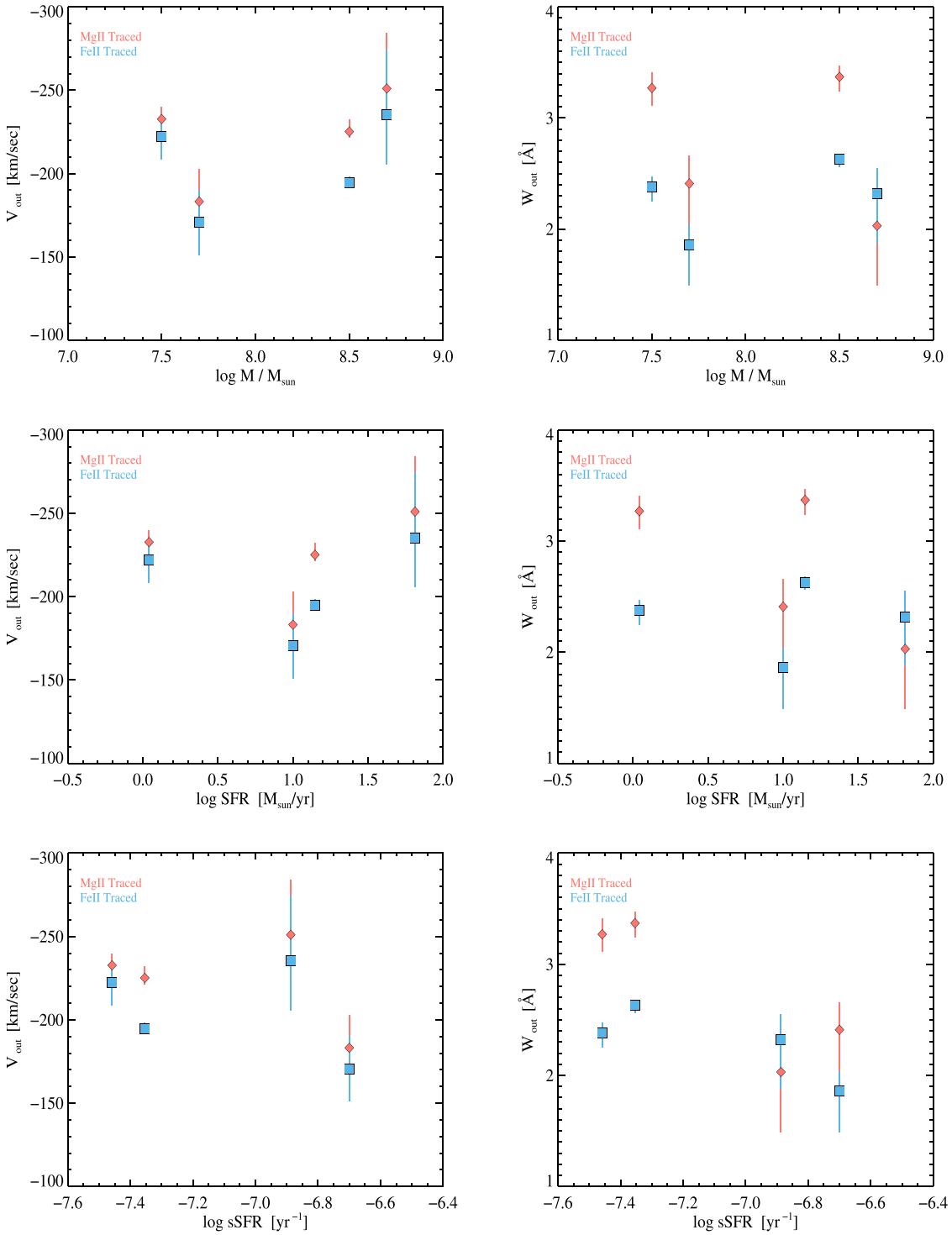

Figure 5. Variation of blueshifted Mg II and Fe II absorption kinematics (left-hand panels) and equivalent widths (right-hand panels) as a function of stellar mass (top panels), SFR (middle panels) and sSFR (bottom panels) of the individual knots, respectively. Outflow velocities traced by blueshifted Mg II absorption (red diamonds) and Fe II absorption (blue squares), show weak trends with increasing star formation rate and stellar mass of the knots.

Mg II emission equivalent width decreases with increasing $\Sigma_{\rm SFR}$, while the Fe II emission equivalent widths show no trend with $\Sigma_{\rm SFR}$. The decrease of Mg II emission equivalent width with increasing $\Sigma_{\rm SFR}$ might be due to higher emission filling for weaker outflows. We see no trend between emission velocities and $\Sigma_{\rm SFR}$ of local knots.

4.2.2 *Outflows traced by Mg II and Fe II*

There have been many studies that have looked into the correlation of $\langle\Sigma_{\rm SFR}\rangle$ with the average blueshifted outflowing gas for the entire galaxy. At low redshifts, Chen et al. (2010) used stacked NaD absorption lines of star-forming galaxies, and found that the outflow

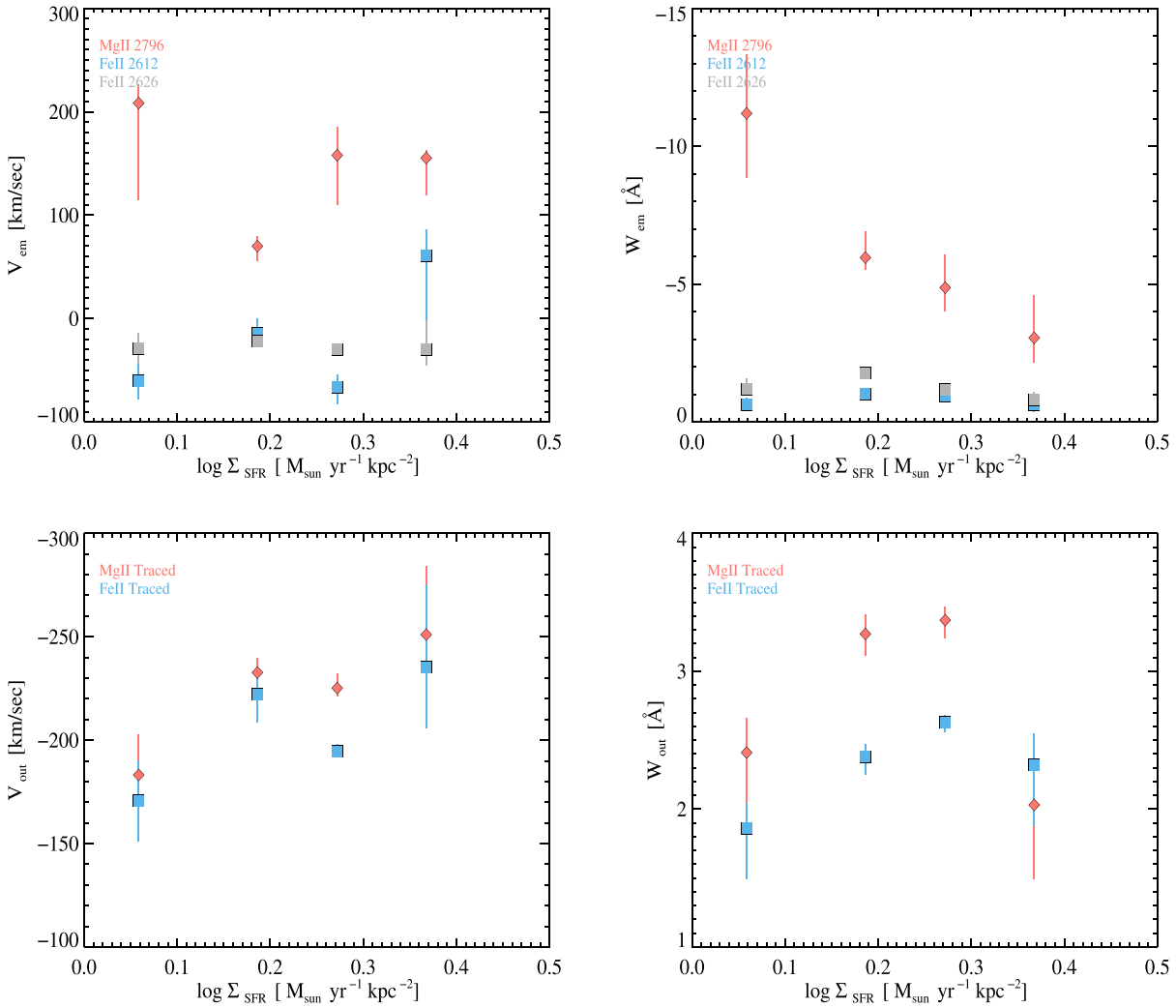

Figure 6. Variation of outflow absorption and emission properties as a function of star formation rate surface density (Σ_{SFR}) of the individual knots. Outflow velocity increases for increasing Σ_{SFR}. Mg II resonant emission equivalent width decreases with increasing Σ_{SFR}.

NaD equivalent width strongly depends on the average Σ_{SFR} of their host galaxies. At $z \sim 1$, Kornei et al. (2012) reported a 3.1σ correlation of outflow velocity with Σ_{SFR}. Bordoloi et al. (2014b), using stacked galaxy spectra found that on average below the canonical threshold ($\Sigma_{SFR} = 0.1\ M_\odot\ yr^{-1}\ kpc^{-2}$) star-forming galaxies exhibit little blueshifted absorption at $z \sim 1$. At $z \sim 2$, Newman et al. (2012) reported a Σ_{SFR} threshold of $1\ M_\odot\ yr^{-1}\ kpc^{-2}$, above which $M^* > 10^{10}\ M_\odot$ galaxies might have stronger outflows as compared to the low-mass galaxies.

In this paper, we look at how outflow properties vary in the 'same' galaxy as a function of the local Σ_{SFR} of the star-forming regions. In Fig. 6, the bottom panels show the variation of outflow velocities and equivalent widths with Σ_{SFR}. The red diamonds are measurement traced by Mg II absorption and the blue squares are measurements traced by Fe II absorption. The outflow velocities show a weak trend of increasing outflow velocities with increasing Σ_{SFR}. A Pearson linear rank correlation test shows a 2.4σ correlation between log Σ_{SFR} and outflow velocities. This finding should be discussed in the context of the canonical SFR surface density 'threshold' of $\Sigma_{SFR} = 0.1\ M_\odot\ yr^{-1}\ kpc^{-2}$. It has been argued that this is the minimum Σ_{SFR} required for driving outflows in local starburst (Heckman 2002; Heckman et al. 2015). Though we lack the dynamic range in Σ_{SFR} to probe below this canonical threshold, we still notice a trend of increasing outflow velocities with localized Σ_{SFR}. It should be noted that other studies observing the effect of Σ_{SFR} on outflow properties have always used global flux-averaged Σ_{SFR} measurements, as they could not resolve the individual star-forming knots and the outflows separately. Here we are discussing the local Σ_{SFR} properties of individual star-forming regions and the associated outflow velocities with these regions. Our findings are consistent with the $z \sim 2$ Newman et al. (2012) results. However our current work is the first study that is observing the effects of Σ_{SFR} and outflow velocities on sub-kpc scales within galaxies (≤ 200 pc; Wuyts et al. 2014) scale.

4.3 Pixel velocity distribution of outflowing gas

In this section, we examine the pixel velocity distribution of the blueshifed Mg II absorption. This approach allows us to probe the low column density, high-velocity tail of the outflowing gas, as well as the bulk of the blueshifted gas as in Section 5. We use the fitted Mg II outflow absorption profile and compute the cumulative velocity distribution of the profile from $0\ km\ s^{-1}$ to $-800\ km\ s^{-1}$. Fig. 7 shows the cumulative pixel velocity distribution for the best

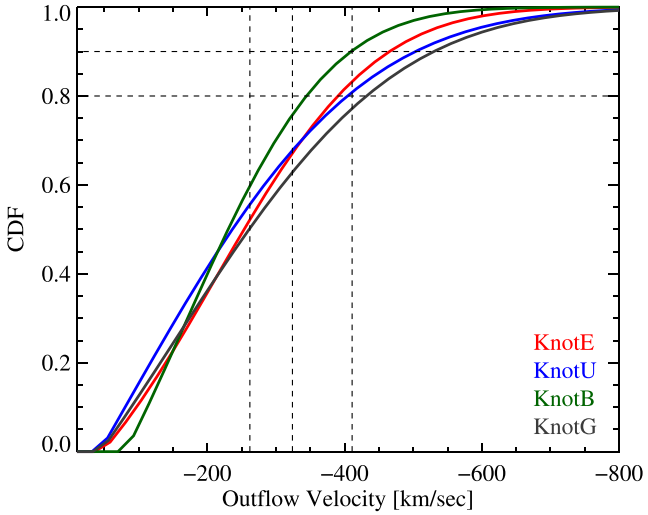

Figure 7. Cumulative outflow pixel velocity distribution function examining how outflowing gas profiles vary. The horizontal dashed lines mark the velocities which contain 80 per cent and 90 per cent of the blueshifted absorption, respectively. Bulk of the blueshifted outflowing absorption is confined within $-400\,\mathrm{km\,s^{-1}}$ for all cases. In case of Knot B, which exhibit the smallest $\Sigma_{\rm SFR}$, 90 per cent of the blueshifted absorption occurs below $-400\,\mathrm{km\,s^{-1}}$. The vertical dashed lines represent the escape velocity from the gravitational potential of the halo at $R = 5$, 20 and 50 kpc, respectively. Almost 20 per cent–50 per cent of the blueshifted absorption has high enough velocity to escape.

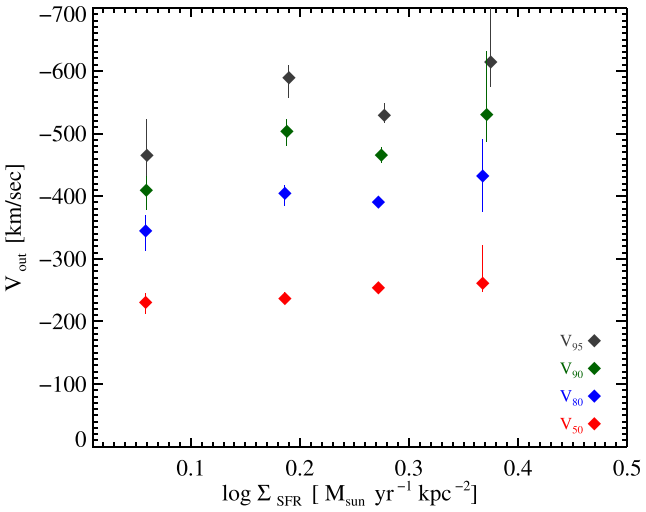

Figure 8. Variation of cumulative outflow velocities with $\Sigma_{\rm SFR}$ when the velocities account for 50 per cent blueshifted absorption (red diamonds), 80 per cent absorption (blue diamonds), 90 per cent absorption (green diamonds), 95 per cent absorption (red diamonds). The dependence of outflow velocity with $\Sigma_{\rm SFR}$ becomes more pronounced as we probe the high-velocity tail of the outflowing gas.

fitting Mg II profiles for each knot. This is an absorption weighted estimate of the amount of gas within a given outflowing velocity. The outflow velocity when the cumulative distribution function is 0.8 gives the maximum velocity below which 80 per cent of the observed Mg II absorption occurs (Fig. 7, dashed line).

We perform a two sample KS test, which rules out the null hypothesis that the pixel velocity distributions for all the knots are drawn from the same parent sample at 0.1 per cent significance level. This effectively tells us that the outflow velocity profiles are different for different star-forming knots at 99.9 per cent confidence. This finding supports the picture that the properties of the galactic outflows, at least in this one $z = 1.7$ galaxy, as being dominated by the properties of the nearest star-forming knots or star clusters rather than the global properties of the galaxies.

To estimate the absorption-weighted uncertainties on this cumulative velocity distribution, we compute the cumulative pixel velocity distribution for each realization of the MCMC chain. The mean velocity and the 1σ velocity spread per pixel gives the estimated mean cumulative velocity and its uncertainty for each pixel. At the highest velocities, the uncertainties in mean velocity estimates rise, as they contain little absorption. Fig. 8 shows the cumulative outflow velocities as a function of galaxy properties when these velocities account for 50 per cent (red diamonds), 80 per cent (blue diamonds), 90 per cent (green diamonds), and 95 per cent (black diamonds) of the total blueshifted absorption, respectively. We see that the difference of outflow velocities between the knots with lowest and highest $\Sigma_{\rm SFR}$ become more pronounced as we probe the higher velocity tail of the outflowing gas. All the knots have outflow velocities $> 300\,\mathrm{km\,s^{-1}}$ for the top 20 per cent of the outflowing pixels (blue diamonds). For all the knots, the bulk of the absorption (≈ 80 per cent), occurs within $400\,\mathrm{km\,s^{-1}}$ of the systemic velocity of the galaxy. The escape velocities for the potential well of this galaxy at $R = 5$, 20 and 50 kpc are given as 411 ± 74, 324 ± 59 and $262 \pm 48\ \mathrm{km\,s^{-1}}$, respectively. These are shown as the vertical dashed lines in Fig. 8. We see that $\approx$ 20–50 per cent of the blueshifted absorption may escape the potential well of the halo.

4.4 Spatial extent of Mg II emission region

We now estimate the spatial extent of Mg II emission observed in these star-forming knots. We use the two-dimensional spectra to estimate how spatially extended are the observed Mg II emission regions. The galaxy RCS0327 is $\sim$ 15 kpc across along the long dimension (see fig. 5 of Wuyts et al. 2014). As discussed in Section 2 and shown in Fig. 1, because the slit was rotated to track the parallactic angle, the observations cover a wide range of position angles in the image plane. Hence we cannot use the co-added two-dimensional spectrum of each knot to estimate spatial extent of Mg II emission. Instead, we perform this analysis on each exposure, since each exposure has a fixed position angle. Only in Knot U and Knot E, and only for the Mg II emission doublet, is the S/N high enough to meaningfully measure the spatial extent of the emission.

In the two-dimensional spectrum of each exposure, we measure the FWHM of the emission line along the spatial direction, summing over 5 pixels in the dispersion direction. We do the same for the nearby continuum emission, summing over 10 pixels in the dispersion direction. To translate these measurements from the image plane to the source plane, we do the following. For each exposure, we identify two points in the image plane that are located along the slit position angle, bracket the knot in question, and are located one FWHM apart as measured from the two-dimensional spectrum. We transform these image plane coordinates to the source plane, measure the distance between them, and call this the equivalent FWHM in the source plane. Fig. 9 illustrates that this linear approximation to the curved footprint of each slit in the source plane is adequate for the small sub-arcsecond scales over which the Mg II emission is spatially extended. Fig. 9 also shows that while the observations covered a wide range of position angles in the image plane, they are compressed to a much narrow range of position angles in the source plane.

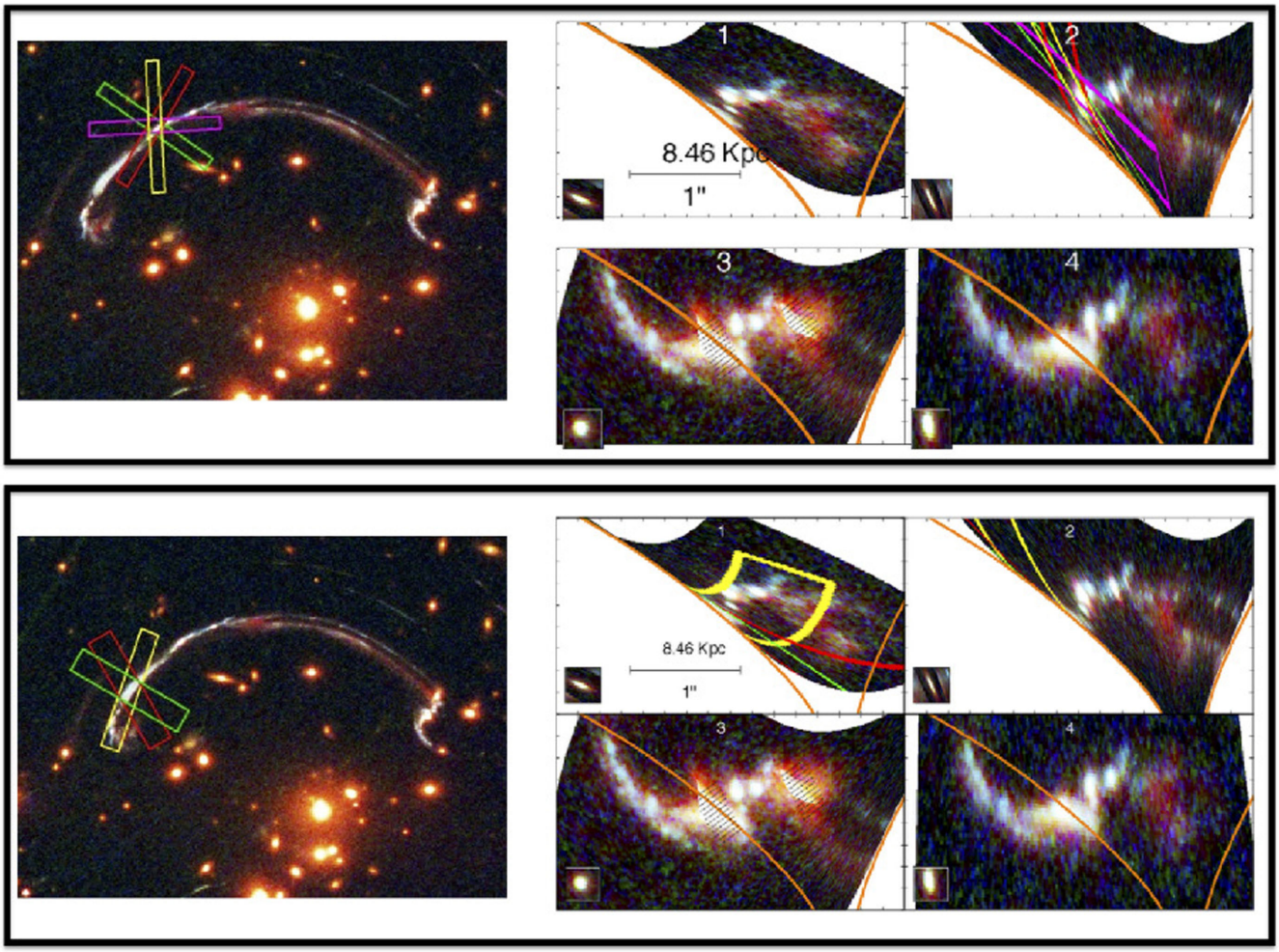

Figure 9. Top-left panel: composite *HST* image of RCSGA 032727-132609, highlighting representative position angles for the MagE observations that targeted Knot E. Top-right panels: source-plane reconstructions for each of the four magnified images of RCSGA 032727-132609. Each sub-panel is marked with the image number, which corresponds to the labels of the multiple images in Fig. 1. The representative MagE slits (pink, green, yellow, and red rectangles in the top-left panel) are mapped to the source plane in the sub-panel for Image 2. The hashed region in the source plane for image 3 marks contamination from two cluster galaxies, G1 and G2. An orange line shows the source-plane caustic. Bottom panels: same as top, but for Knot U. This figure is adapted from fig. 3 of Sharon et al. (2012).

Rubin et al. (2011) chose to subtract the continuum emission from the two-dimensional spectrum, then fit the residual line emission to a seeing-blurred model. In our case, the continuum subtraction is negligible, as the line flux is much stronger per pixel than the continuum flux. Rubin et al. (2011) also dealt with a spatially resolved galaxy. By contrast, our target star-forming knots are effectively unresolved in the slit spatial direction. Therefore, we use the continuum FWHM as a proxy for the seeing, and by subtracting in quadrature the continuum FWHM from the observed Mg II emission line FWHM, we estimate the spatial extent of the Mg II emission.

For Knot E, in 9 out of 10 exposures, the FWHM of Mg II 2796, and in 7 out of 9 cases for Mg II 2803, emission is larger than the FWHM of the continuum. (In one additional exposure, the emission profile is too noisy to fit.) For Knot U, in 8 out of 10 exposures the FWHM of Mg II 2796 emission is larger than that of the continuum. (Two other exposures have contaminating emission from other knots in the slit, and are therefore ignored.) We find a mean FWHM and error in the mean for Mg II 2796 of 0.34 ± 0.06 arcsec (2.9 ± 0.5 kpc) for Knot E, and 0.30 ± 0.05 arcsec (2.6 ± 0.4 kpc) for Knot U, both in the source plane. Hence the spatial extent up to which almost all the light from Mg II emission is seen (5σ of the mean FWHM) is given as $R = 6.16 \pm 0.5$ kpc for Knot E and $R = 5.52 \pm 0.4$ kpc for Knot U, respectively.

Thus, in the spectra of Knot U and Knot E, the bulk of the Mg II emission arises within 6 kpc of each knot, with the bulk of emission at smaller radii (∼3 kpc). These are smaller scales than those measured previously in Mg II emission. The field galaxies with the most spatially extended Mg II emission showed radii of 6–11 kpc (galaxy TKRS 4389; Rubin et al. 2011); and ∼11 kpc (galaxy 32016857; Martin et al. 2013). The stacked spectrum of Erb et al. (2012) showed an excess at radii of 7 kpc.

Thus, the Mg II emission in RCS0327 is extended on kpc scales, but the emission is confined to smaller radii than seen previously in two galaxies and in a stack of 33 galaxies. These results are not necessarily in conflict. Afterall, the two galaxies of Rubin et al. (2011) and Martin et al. (2013) were selected because they showed the most extended Mg II emission of their respective samples. While the Mg II emission in RCS0327 is more compact than in the Erb et al. (2012) stack, the distribution of size scales within that stack is

unknown; that is, after all, a limitation of stacking, and motivation for obtaining measurements in individual galaxies.

4.5 Minimum mass outflow rate

In this section we report the minimum mass outflow rates for RCS0327. The mass outflow rate estimates are highly uncertain and depend on the assumed geometry of the outflowing gas. We always assume a this shell geometry to estimate the mass outflow rates. As discussed in Section 3, our models fit the observations with typical outflow column densities of $N_{\rm flow} \gtrsim 10^{14}$ cm^{-2} for Mg II and $N_{\rm flow} \gtrsim 10^{14.2}$ cm^{-2} for Fe II. We estimate a conservative lower limit on the total hydrogen column density of the outflowing gas by assuming no ionization correction ($N_{\rm Mg\,II} = N_{\rm Mg}$; $N_{\rm Fe\,II} = N_{\rm Fe}$) and assume the minimum estimated column density for both Mg II and Fe II with no correction for line saturation. The nebular oxygen abundances for the clumps fall in the range of $8.02 \lesssim 12 + \log(O/H) \lesssim 8.28$ (Wuyts et al. 2014). This implies that the ISM of RCS0327 has abundances close to 27 per cent solar values (Solar abundance = 8.7; Allende Prieto, Lambert & Asplund 2001), with a spread of ≈0.08 dex. Since the cool outflowing gas is likely to be entrained material swept up from the ISM, we adopt the ISM metallicity to be the metallicity of the cool outflowing gas. We assume a factor of −1.3 dex of Mg depletion on to dust and a factor of −1.0 dex of Fe depletion on dust (Jenkins 2009). This allows us to estimate a lower limit of N_H column densities for each knot. Using this we can compute the mass outflow rate for a wind with opening angle $\Omega_{\rm w}$ and outflow velocity v as

$$\dot{M}_{\rm out} = \Omega_{\rm w} C_f C_\Omega \mu m_p N_H R v. \quad (4)$$

Here C_Ω is the angular covering fraction and C_f is the clumpiness covering fraction, μm_p is the mean atomic weight and R is the spatial extent of the outflowing gas. Large-scale galactic outflows are not spherical; but are preferentially observed along the minor axis of galaxies with an opening angle of ≈ 50°–55°(Martin et al. 2012; Bordoloi et al. 2014b; Rubin et al. 2014). However, we are looking at local star-forming regions inside the galaxy, where it is safe to assume that gas is being swept up in spherical shells (Heckman 2002). Hence we set the outflow angle $\Omega_{\rm w} = 4\pi$ (thin shell approximation) and assume a smooth outflow ($C_f C_\Omega = 1$). Setting $\mu = 1.4$, we rewrite the mass outflow rate for a thin shell geometry as (see Weiner et al. 2009)

$$\dot{M}_{\rm out} \gtrsim 22\,{\rm M}_\odot\,{\rm yr}^{-1} \frac{N_H}{10^{20}\,{\rm cm}^{-2}} \frac{R}{5\,{\rm kpc}} \frac{v}{300\,{\rm km\,s}^{-1}}. \quad (5)$$

The spatial extent (R) to be used to calculate the mass outflow rate depends upon the assumed model for the absorbing gas. In the idealized case of a thin shell-like structure, it is simply the radius of that shell. Constraining R of the outflowing gas in absorption is not trivial. Down-the-barrel observation of galaxies can detect outflowing gas at any location along the line of sight to the target galaxy including material which is tens of kiloparsecs away from the host galaxy. Using stacked spectra of ≈ 4000 galaxies, Bordoloi et al. (2011) have shown that outflowing gas traced by Mg II absorption can be detected out to ≳ 50 kpc of the host galaxy at $z \sim 0.7$. However, most of such Mg II absorbers at impact parameters > 20 kpc have equivalent widths < 2 Å. Our outflow equivalent widths are typically ≳ 2 Å. Small numbers of such strong galaxy-absorber pairs are observed at impact parameters of ≈ 50 kpc (e.g. Nestor et al. 2007). However, these surveys may misidentify the true galaxy counterparts if the emission from the host galaxy is blended with the bright QSO emission or is below the detection limit of the survey.

Table 4. Minimum mass outflow rates for each star-forming knots. η gives the lower limits on the mass loading factor for each knot as traced by Mg II and Fe II transitions, respectively.

Knot	Mass outflow rates [M$_\odot$ yr^{-1}] Mg II traced	Fe II traced	$\eta_{\rm Mg\,II}$	$\eta_{\rm Fe\,II}$
Knot E	30	33	2.1	2.4
Knot U	51	66	46	60.
Knot B	34	41	3.4	4.1
Knot G	41	78	0.64	1.2

Hence, we assume a conservative estimate for the spatial extent of the outflowing gas by assuming that the densest part of the outflowing gas can be traced by the spatial extent of the resonant Mg II emission lines. We assume the spatial extent of the Mg II emission lines estimated in Section 6 is the spatial extent of the outflowing gas. Since we only have information on Knot E ($R = 6.2$ kpc) and Knot U ($R = 5.5$ kpc), we assume that Knot B and Knot G have the same spatial extent as Knot E.

Given the uncertainties above, we note that the mass outflow rate calculations are highly uncertain and model dependent, and should only be taken as rough back of the envelope estimates, prone to systematic uncertainties. With that caveat in mind, we report the minimum mass outflow rates below. The minimum mass outflow rate estimate for Knot E traced by the Mg II transition as >30 M$_\odot$ yr^{-1} and by the Fe II transition as >33 M$_\odot$ yr^{-1}. The minimum mass outflow rate estimate for Knot G is given by the Mg II transition as >41 M$_\odot$ yr^{-1} and by the Fe II transition as >78 M$_\odot$ yr^{-1}. The mass outflow rates are tabulated in Table 4. Any such estimate of mass outflow rate is strictly a lower limit as we are neglecting any ionization correction and underestimating any effects of saturation. The true mass outflow rate could be easily a factor of 10 higher than these observed values. These values are consistent with the values derived by Martin et al. (2012). We find that the mass outflow rates are greater than the typical SFR of the individual knots and we can put lower limits on the mass loading factor η ($\dot{\rm M}_{\rm out} = \eta$ SFR). As an example; we find that $\eta_{\rm Mg\,II}$ for Knot E is > 2.1 and for Knot G is >1. These mass loading factor estimates are consistent with the findings of Newman et al. (2012) at $z \sim 2$. They estimate a mass loading factor of ≈2 for their M∗ > 10^{10} M$_\odot$ galaxies. All the mass outflow rate estimates are tabulated in Table 4.

4.6 Comparison with local starburst galaxies

In this section, we will compare the observed outflow properties in RCS0327 with that for local starburst galaxies and compare them with a simple idealized analytical momentum-driven wind model from Heckman et al. (2015). They studied a sample of 39 local starburst galaxies, and used *HST*/COS and FUSE observations to estimate the outflow velocities and mass outflow rates for these galaxies. The grey points in Fig. 10 show these measurements. It should be noted that the mass outflow rate calculations are highly uncertain and should only be taken as roughly indicative estimates. We are assuming a statistical uncertainty on $\log \dot{M}_{\rm out}$ of 0.3 dex, similar to Heckman et al. (2015) for comparison.

Fig. 10, top-left panel shows the relationship between mass outflow rates and SFR of these starburst galaxies (grey points). The mass outflow rates estimated in different regions of one $z = 1.7$

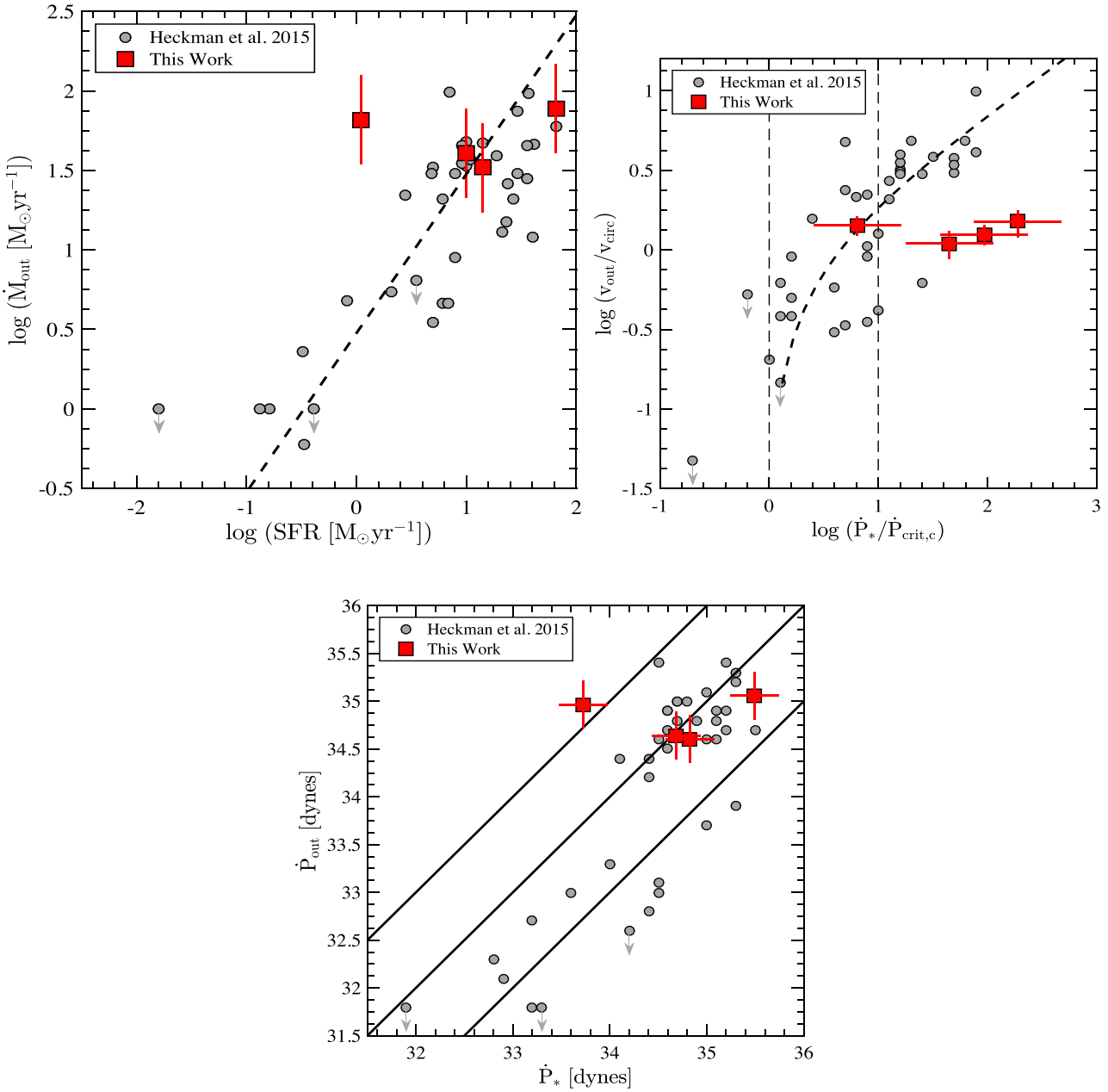

Figure 10. Top-left panel: mass outflow rate estimates plotted as a function of star formation rates. The grey points show the mass outflow rates for local starburst galaxies from Heckman et al. 2015. The red points are mass outflow rates estimated in this work for individual star-forming knots in one $z = 1.7$ galaxy. The dashed line shows the mass outflow rate when the mass loading factor η =3. Top Right-hand panel: the observed normalized outflow velocities ($v_{\rm out}/v_{\rm circ}$) as a function of the ratio of the amount of momentum flux supplied by the starburst to the critical value needed to overcome gravity and drive an outflow. The local starburst galaxies (grey points) exhibit a range of momentum flux ratio driving outflows. The individual star-forming knots of a single high z galaxy (red squares) have a range of momentum fluxes driving outflows, comparable to a set of starburst galaxies. The dashed line is from the equation of motion for a momentum driven cloud model. The vertical dashed lines show the ratio of $\dot{P}_*/\dot{P}_{\rm crit} = 1$ and 10. Bottom panel: outflow momentum flux estimates as a function of rate of momentum supplied by the starburst. The diagonal lines show the ratios of $\dot{P}_{\rm out}/\dot{P}_* = 10$, 1.0 and 0.1. The outflows driven by individual star-forming knots (red squares) are carrying the full momentum supplied by the starburst (see the text).

galaxy (red squares) shows similar variation as seen in local starburst galaxies. For these estimates, we find that the typical η within a galaxy can vary from 1 to 4 times the local SFR.

We estimate the momentum flux carried out by the outflowing gas as $\dot{P}_{\rm out} = \dot{M}_{\rm out} v_{\rm out}$ dynes. These values are listed in Table 5. We further estimate the total momentum flux supplied by a typical starburst due to a combination of hot wind fluid driven by the ejecta of massive stars and the radiation pressure. We follow Heckman et al. (2015), and adopt an expression based on STARBURST99 (Leitherer et al. 1999) and write the total momentum flux in a starburst as $\dot{P}_* = SFR \times 4.8 \times 10^{33}$ dynes. Fig. 10, bottom panel, shows the distribution of momentum flux carried by the outflow and the total momentum flux in a starburst, for local starbursts (grey points) and this work (red squares). This shows that almost all of the momentum flux ($\sim$ 100 per cent) supplied by the star-forming knots are being carried out by the observed outflows. Outflows driven by individual

Table 5. [1]The momentum flux in the outflows. The uncertainties will be dominated by mass outflow rate estimates. [2] The momentum flux from starburst proportional to the star formation rate (see the text). The uncertainties are hard to quantify (Leitherer et al. 1999). [3] The critical momentum flux in a starburst that is required to escape gravity for a cloud at the radius of the star-forming knots.

Knot	Momentum Flux		
	log $\dot{P}^1_{\rm out}$ (log dynes)	log $\dot{P}^2_{*}$ (log dynes)	log $\dot{P}^3_{\rm crit,c}$ (log dynes)
Knot E	34.6	34.8	32.9
Knot U	34.9	33.7	32.9
Knot B	34.6	34.7	33.0
Knot G	35.0	35.5	32.2

star-forming knots are as forceful as the outflows driven by local starbursts ($\dot{P}_{\rm out} > 10^{34}$ dynes; Heckman et al. 2015).

We now compare the data to a simple analytical model described in Heckman et al. (2015). This model assumes that absorption lines are produced by a distribution of clouds that are being driven out of the galaxy by the momentum supplied by a starburst as described above. Following Heckman et al. (2015), we define a critical momentum flux which is needed for gas clouds to escape the local star-forming regions of radius r_* given as $\dot{p}_{\rm crit} = 4\pi r_* N_{\rm c} \langle m \rangle v^2_{\rm circ}$. Here r_* is the size of the star-forming knots (Wuyts et al. 2014) and the values are listed in Table 5. $N_{\rm c}$ is the cloud neutral hydrogen column density.

Fig. 10, top-right panel shows the normalized outflow velocities ($v_{\rm out}/v_{\rm circ}$) as a function of the ratio of the amount of momentum flux supplied by the starburst to the critical value needed to overcome gravity and drive an outflow ($\dot{p}_*/\dot{p}_{\rm crit}$) for local starbursts (grey points) and this work (red squares). We estimate the outflow velocity for this model from equation 5 of Heckman et al. (2015), and this is shown as the dashed line. As compared to the local starbursts, outflows driven from this one $z = 1.7$ galaxy produces stronger outflows ($\dot{p}_*/\dot{p}_{\rm crit} \gtrsim 10.$). However the normalized outflow velocities saturate for the strongest outflows. Bulk of the mass observed in these stronger outflows at $z = 1.7$ exceed the escape velocity of the halo. If we underestimate $\dot{p}_{\rm crit}$, as the values of $N_{\rm c}$ is uncertain, the ratio $\dot{p}_*/\dot{p}_{\rm crit}$ will change and the red squares in Fig. 10, top-right panel will be more consistent with the local observations.

In RCS0327 the knot-to-knot variations in mass outflow rates, momentum flux and $\dot{p}_*/\dot{p}_{\rm crit}$ are comparable to that observed in a sample of starburst galaxies in the local Universe. This certainly need not have been the case; if the observed outflows were well mixed and large (>>1 kpc), we would have measured the same properties for each knot. We thus conclude that, at least in this one galaxy, we are seeing a 'locally sourced outflows', i.e. the outflow properties are determined locally by nearby star-forming regions, and are not uniform on kiloparsec scales.

5 CONCLUSIONS

In this paper, we present the rest-frame ultraviolet spectra of Mg II and Fe II emission and absorption lines along four lines of sight separated by up to 6 kpc in a gravitationally lensed $z = 1.70$ galaxy, targeting four bright regions. Such observations are challenging, and only possible with current telescopes with the assistance of strong gravitational lensing and a favourable lensing configuration. While RCS0327 is one of the brightest lensed galaxies known, there are hundreds of fainter lensed galaxies in which this experiment could be repeated with upcoming 20–30 m ground-based optical telescopes. The main findings of this work are as follows.

(i) All four individual star-forming knots are driving outflows traced by blueshifted Mg II and Fe II absorption profiles. The outflow velocities traced by blueshifted Mg II absorption range from $\approx -183\,{\rm km\,s^{-1}}$ to $-251\,{\rm km\,s^{-1}}$; and outflow velocities traced by blueshifted Fe II absorption range from $\approx -171\,{\rm km\,s^{-1}}$ to $-235\,{\rm km\,s^{-1}}$. The rest-frame Mg II outflow equivalent widths range from 2.03 to 3.37 Å; and the rest-frame Fe II outflow equivalent widths range from 1.86 to 2.63 Å, respectively.

(ii) Individual star-forming knots with higher local SFR surface densities ($\Sigma_{\rm SFR}$) exhibit higher outflow velocities. This is consistent with the picture of outflows being driven due to local star formation activity in star clusters. We find a 2.4σ correlation between outflow velocities and the $\Sigma_{\rm SFR}$ of the individual knots.

(iii) We detect resonant Mg II emission in all the four spectra studied in this paper. The Mg II emission velocity centroids are always redshifted relative to the systemic zero velocity of the individual knots. This is consistent with the scenario that the physical origin of the Mg II emission doublet is in photons scattering off the backside of galactic winds.

(iv) Star-forming knots with smaller $\Sigma_{\rm SFR}$ exhibit the strongest Mg II emission equivalent widths. Knot G with the highest $\Sigma_{\rm SFR}$, exhibits a Mg II emission equivalent width ~ 3.7 times smaller than Knot B; which has the lowest $\Sigma_{\rm SFR}$ of all the four knots.

(v) We detect Fe II 2612, 2626 fluorescence emission lines for all the four knots whereas we do not detect any resonant Fe II emission lines. The Fe II 2612, 2626 emission lines are either slightly blueshifted or are consistent with the systemic zero velocities of the individual clumps.

(vi) We estimate the spatial extent of the Mg II emission lines from the extended two-dimensional emission profile. We estimate the FWHM of the extended Mg II 2796 emission at the source plane to be 0.34 ± 0.06 arcsec (2.9 ± 0.5 kpc) for Knot E, and 0.30 ± 0.05 arcsec (2.6 ± 0.4 kpc) for Knot U, respectively.

(vii) Assuming a thin shell geometry, we estimate the minimum mass outflow rates ($\dot{M}_{\rm out}$), which range from > 30 to $>51\,{\rm M_\odot\,yr^{-1}}$ as estimated from Mg II absorption and > 33 to $>78\,{\rm M_\odot\,yr^{-1}}$ as estimated from Fe II absorption. These are conservative lower limits as we are not accounting for line saturation and ionization corrections. Assuming $\dot{M}_{\rm out} \propto$ SFR, we find that the mass loading factor η is a few times the SFR of the individual star-forming knots. This is the first time that ηs have been measured for multiple individual regions within the same galaxy in the distant Universe, and is a crucial observable to models of how galaxies process their gas.

(viii) Given the low circular velocity inferred for two galaxies with the stellar mass of the merging pair of galaxies RCS0327; almost 20–50 per cent of the blueshifted absorption may escape the gravitational potential of the galaxy.

(ix) The knot-to-knot variations in mass outflow rates, momentum flux and $\dot{p}_*/\dot{p}_{\rm crit}$ in RCS0327 are comparable to starburst galaxies in local Universe. This is the first comparison of mass loading factor and wind momentum in outflows at z ∼ 2 to outflows in the local Universe. The observed knot to knot variation in these quantities argues for the importance of localized sources in the galaxies in driving outflows in the Universe.

The spectra for RCS0327 show that Mg II emission is occurring across the galaxy, but that the properties of the outflow are heavily influenced by the nearest star-forming regions. Mg II emission is seen in each of the four knots we targeted, separated by up to 6 kpc. In the two knots with high S/N spectra, the Mg II emission is more

spatially extended than the continuum, out to 6 kpc scales. It is clearly not the case that only one region is producing all the Mg II emission in this galaxy. However, (Section 4.2) the outflow properties correlate with the nearest star-forming region, and (Section 4.3) the outflow velocity profile varies from knot to knot, across separations of 0.4 to 6 kpc in the source plane (see fig. 5 of Wuyts et al. 2014). Thus, while the emission in RCS0327 extends out to ∼6 kpc from knots E and U, the bulk of the emission arises from <3 kpc, on the same scale as the ∼2 kpc spacing between knots. Thus, though the outflow in RCS0327 does extend to galaxy-wide scales, the properties of the outflow appear to be shaped most strongly by the closest star-forming complex.

From knot to knot, we find large variations in the strength of the Mg II emission, the velocity peak of that emission, and in the velocity profiles of the inferred outflows. In RCS0327, the outflowing winds appear quite different on lines of sight separated by only a few kiloparsecs. This did not have to be the case; if the outflow were well-mixed and large, >>1 kpc, we would have measured the same outflow properties for each knot. That is very different from what we observed. We thus conclude that, at least in this one galaxy, we are seeing 'locally sourced outflows' – the outflows must be close to the star-forming regions, and still bear the velocity signatures of the gas flowing out of those regions, such that the different sight lines encounter quite different outflows. At least in this one galaxy, the outflow properties are determined locally by nearby star-forming regions, and are not uniform on kiloparsec scales. Repeating this experiment in other lensed galaxies with multiple sight lines will test the universality of this result. If they also show significant line of sight variation, then it will be clear that studies of outflows in distant galaxies must spatially resolve them.

ACKNOWLEDGEMENTS

RB would like to thank the Aspen Center for Physics (supported by NSF grant 1066293) for hospitality and productive atmosphere and organizers of the workshop 'Physics of Accretion and Feedback in the Circum-Galactic Medium' in 2015 June, for opportunities to discuss results presented here during completion of this paper. RB would like to thank Timothy Heckman for stimulating discussions on this work. RB would also like to thank Peter Behroozi for providing mock catalogues to estimate halo mass of the host galaxy. Partial support for this work was provided by NASA through Hubble Fellowship grant #51354 awarded by the Space Telescope Science Institute, which is operated by the Association of Universities for Research in Astronomy, Inc., for NASA, under contract NAS 5-26555. This paper includes data gathered with the 6.5 m Magellan Telescopes located at Las Campanas Observatory, Chile. Magellan observing time for this programme was granted by the telescope allocation committees of the Carnegie Observatories, the University of Chicago, the University of Michigan, and Harvard University.

REFERENCES

Adelberger K. L., Shapley A. E., Steidel C. C., Pettini M., Erb D. K., Reddy N. A., 2005, ApJ, 629, 636
Allende Prieto C., Lambert D. L., Asplund M., 2001, ApJ, 556, L63
Asplund M., Grevesse N., Sauval A. J., Scott P., 2009, ARA&A, 47, 481
Behroozi P. S., Wechsler R. H., Wu H.-Y., 2013, ApJ, 762, 109
Bell E. F., McIntosh D. H., Katz N., Weinberg M. D., 2003, ApJS, 149, 289
Binney J., Tremaine S., 1987, Galactic Dynamics. Princeton Univ. Press, Princeton, NJ
Blanton M. R. et al., 2003, ApJ, 592, 819
Bordoloi R. et al., 2011, ApJ, 743, 10
Bordoloi R., Lilly S. J., Kacprzak G. G., Churchill C. W., 2014a, ApJ, 784, 108
Bordoloi R. et al., 2014b, ApJ, 794, 130
Bordoloi R. et al., 2014c, ApJ, 796, 136
Brammer G. B. et al., 2011, ApJ, 739, 24
Calzetti D., Kinney A. L., Storchi-Bergmann T., 1994, ApJ, 429, 582
Chabrier G., 2003, PASP, 115, 763
Chen Y.-M., Tremonti C. A., Heckman T. M., Kauffmann G., Weiner B. J., Brinchmann J., Wang J., 2010, AJ, 140, 445
Coil A. L., Weiner B. J., Holz D. E., Cooper M. C., Yan R., Aird J., 2011, ApJ, 743, 46
Cooksey K. L., Thom C., Prochaska J. X., Chen H.-W., 2010, ApJ, 708, 868
Daddi E. et al., 2007, ApJ, 670, 156
Davé R., Finlator K., Oppenheimer B. D., 2012, MNRAS, 421, 98
Erb D. K., Quider A. M., Henry A. L., Martin C. L., 2012, ApJ, 759, 26
Faber S. M. et al., 2007, ApJ, 665, 265
Förster Schreiber N. M. et al., 2014, ApJ, 787, 38
Gabor J. M., Davé R., Oppenheimer B. D., Finlator K., 2011, MNRAS, 417, 2676
Genzel R. et al., 2014, ApJ, 796, 7
Giavalisco M. et al., 2011, ApJ, 743, 95
Gilbank D. G., Gladders M. D., Yee H. K. C., Hsieh B. C., 2011, AJ, 141, 94
Haario H., Saksman E., Tamminen J., 2001, Bernoulli, 7, 223
Heckman T. M., 2002, in Mulchaey J. S., Stocke J. T., eds, ASP Conf. Ser. Vol. 254, Extragalactic Gas at Low Redshift. Astron. Soc. Pac., San Francisco, p. 292
Heckman T. M., Lehnert M. D., Strickland D. K., Armus L., 2000, ApJS, 129, 493
Heckman T. M., Alexandroff R. M., Borthakur S., Overzier R., Leitherer C., 2015, ApJ, 809, 147
Jenkins E. B., 2009, ApJ, 700, 1299
Kassin S. A. et al., 2012, ApJ, 758, 106
Kennicutt R. C., Jr, 1998, ARA&A, 36, 189
Kinney A. L., Bohlin R. C., Calzetti D., Panagia N., Wyse R. F. G., 1993, ApJS, 86, 5
Klypin A. A., Trujillo-Gomez S., Primack J., 2011, ApJ, 740, 102
Kornei K. A., Shapley A. E., Martin C. L., Coil A. L., Lotz J. M., Schiminovich D., Bundy K., Noeske K. G., 2012, ApJ, 758, 135
Kornei K. A., Shapley A. E., Martin C. L., Coil A. L., Lotz J. M., Weiner B. J., 2013, ApJ, 774, 50
Kurucz R. L., 2005, Mem. Soc. Astron. Ital. Suppl., 8, 14
Lehnert M. D., Heckman T. M., 1996, ApJ, 462, 651
Leitherer C. et al., 1999, ApJS, 123, 3
Leitherer C., Tremonti C. A., Heckman T. M., Calzetti D., 2011, AJ, 141, 37
Marshall J. L. et al., 2008, in McLean I. S., Casali M. M., eds, Proc. SPIE Conf. Ser. Vol. 7014, Ground-based and Airborne Instrumentation for Astronomy II. SPIE, Bellingham, p. 54
Martin C. L., 2005, ApJ, 621, 227
Martin C. L., Bouché N., 2009, ApJ, 703, 1394
Martin C. L., Shapley A. E., Coil A. L., Kornei K. A., Bundy K., Weiner B. J., Noeske K. G., Schiminovich D., 2012, ApJ, 760, 127
Martin C. L., Shapley A. E., Coil A. L., Kornei K. A., Murray N., Pancoast A., 2013, ApJ, 770, 41
Morton D. C., 2003, ApJS, 149, 205
Murray N., Ménard B., Thompson T. A., 2011, ApJ, 735, 66
Nestor D. B., Turnshek D. A., Rao S. M., Quider A. M., 2007, ApJ, 658, 185
Newman S. F. et al., 2012, ApJ, 761, 43
Noeske K. G. et al., 2007, ApJ, 660, L47
Patel S. G. et al., 2013, ApJ, 766, 15
Pettini M., Shapley A. E., Steidel C. C., Cuby J.-G., Dickinson M., Moorwood A. F. M., Adelberger K. L., Giavalisco M., 2001, ApJ, 554, 981
Prochaska J. X., Kasen D., Rubin K., 2011, ApJ, 734, 24
Rigby J. R., Wuyts E., Gladders M. D., Sharon K., Becker G. D., 2011, ApJ, 732, 59

Rubin K. H. R., Weiner B. J., Koo D. C., Martin C. L., Prochaska J. X., Coil A. L., Newman J. A., 2010, ApJ, 719, 1503
Rubin K. H. R., Prochaska J. X., Ménard B., Murray N., Kasen D., Koo D. C., Phillips A. C., 2011, ApJ, 728, 55
Rubin K. H. R., Prochaska J. X., Koo D. C., Phillips A. C., 2012, ApJ, 747, L26
Rubin K. H. R., Prochaska J. X., Koo D. C., Phillips A. C., Martin C. L., Winstrom L. O., 2014, ApJ, 794, 156
Rupke D. S., Veilleux S., Sanders D. B., 2005, ApJS, 160, 115
Scarlata C., Panagia N., 2015, ApJ, 801, 43
Shapley A. E., Steidel C. C., Pettini M., Adelberger K. L., 2003, ApJ, 588, 65
Sharon K., Gladders M. D., Rigby J. R., Wuyts E., Koester B. P., Bayliss M. B., Barrientos L. F., 2012, ApJ, 746, 161
Tremonti C. A. et al., 2004, ApJ, 613, 898
Tumlinson J. et al., 2011, Science, 334, 948
Veilleux S., Cecil G., Bland-Hawthorn J., 2005, ARA&A, 43, 769
Wark D. Q., Mercer D. M., 1965, Appl. Opt., 4, 839
Weiner B. J. et al., 2009, ApJ, 692, 187
Werk J. K. et al., 2014, ApJ, 792, 8
Whitaker K. E., Rigby J. R., Brammer G. B., Gladders M. D., Sharon K., Teng S. H., Wuyts E., 2014, ApJ, 790, 143
Wu C.-C., Boggess A., Gull T. R., 1983, ApJ, 266, 28
Wuyts E. et al., 2010, ApJ, 724, 1182
Wuyts E., Rigby J. R., Gladders M. D., Sharon K., 2014, ApJ, 781, 61
Zhu G., Ménard B., 2013, ApJ, 770, 130

This paper has been typeset from a TEX/LATEX file prepared by the author.